Check for updates

ADVANCED HEALTHCARE MATERIALS
www.advhealthmat.de

Biocompatibility of Water-Dispersible Pristine Graphene and Graphene Oxide Using a Close-to-Human Animal Model: A Pilot Study on Swine

Paola Nicolussi, Giovannantonio Pilo, Maria Giovanna Cancedda, Guotao Peng, Ngoc Do Quyen Chau, Alejandro De la Cadena, Renzo Vanna, Yarjan Abdul Samad, Tanweer Ahmed, Jeremia Marcellino, Giuseppe Tedde, Linda Giro, Acelya Ylmazer, Federica Loi, Gavina Carta, Loredana Secchi, Silvia Dei Giudici, Simona Macciocu, Dario Polli, Yuta Nishina, Ciriaco Ligios, Giulio Cerullo, Andrea Ferrari, Alberto Bianco, Bengt Fadeel, Giulia Franzoni, and Lucia Gemma Delogu**

Graphene-based materials (GBMs) are of considerable interest for biomedical applications, and the pilot study on the toxicological and immunological impact of pristine graphene (GR) and graphene oxide (GO) using swine as a close-to-human provides valuable insights. First, ex vivo experiments are conducted on swine blood cells, then GBMs are injected intraperitoneally (i.p.) into swine. Hematological and biochemical analyses at various intervals indicate that neither GO nor GR cause systemic inflammation, pro-coagulant responses, or renal or hepatic dysfunction. Importantly, no systemic toxicity is observed. Analysis of a panel of 84 immune-related genes shows minimal impact of GO and GR. The animals are sacrificed 21 days post-injection, and transient absorption imaging and Raman mapping show the presence of GO and GR in the mesentery only. Histological evaluation reveals no signs of alterations in other organs. Thus, clusters of both materials are detected in the mesentery, and GO aggregates are surrounded only by macrophages with the formation of granulomas. In contrast, modest local reactions are observed around the GR clusters. Overall, these results reveal that i.p. injection of GBMs resulted in a modest local tissue reaction without systemic toxicity. This study, performed in swine, provides essential guidance for future biomedical applications of graphene.

1. Introduction

Graphene and its oxidized form, graphene oxide (GO), are carbon-based nanomaterials with several applications in the last decade due to their remarkable physicochemical properties. In biomedicine, their portfolio of applications kept increasing dramatically. GBMs have proven their potential in tissue engineering, drug delivery, biosensing, and as anti-cancer multivalent platforms.[1–4] However, their potential interactions with biological systems deriving from their highly variable physicochemical properties raised concerns regarding their potential risks to human health. A thorough analysis of the biocompatibility of GBMs, considering their complexity in their specificities, has been required before their safe translation for therapeutic and diagnostic applications.[3,5]

In this context, a deep understanding of the interactions of GBMs with the immune system is a prerequisite for their utilization in biomedicine since any exposure to nanomaterials will inevitably lead to the encounter with the immune cells, in particular with phagocytic cells of the innate immune system, such as neutrophils and macrophages, which represent the primary cellular defense to foreign organisms or particles.[6–8] We previously studied how the lateral dimensions and surface functionalization of graphene oxide can impact the activation and interaction of these nanomaterials with several primary human immune cell populations such as monocytes and

The ORCID identification number(s) for the author(s) of this article can be found under https://doi.org/10.1002/adhm.202401783

© 2024 The Author(s). Advanced Healthcare Materials published by Wiley-VCH GmbH. This is an open access article under the terms of the Creative Commons Attribution-NonCommercial License, which permits use, distribution and reproduction in any medium, provided the original work is properly cited and is not used for commercial purposes.

DOI: 10.1002/adhm.202401783

P. Nicolussi, G. Pilo, M. G. Cancedda, G. Tedde, F. Loi, G. Carta, L. Secchi, S. Dei Giudici, S. Macciocu, C. Ligios, G. Franzoni
Istituto Zooprofilattico Sperimentale della Sardegna
Sassari 07100, Italy
E-mail: giulia.franzoni@izs-sardegna.it

B cells.[1,9,10] Nevertheless, such studies are limited because cells cultured in a dish do not comprehensively reflect a human in vivo condition.

Moreover, preclinical mice in vivo studies used graphene oxide in its differently functionalized forms, while comprehensive in vivo studies for pristine graphene are missed.[11,12] The scarcity of in vivo studies involving pristine graphene could be explained by preliminary reports showing its toxicity compared to the functionalized GBMs and graphene oxide, in particular.[13–18] Due to these reasons, pristine graphene has been left out of several biomedical scenarios. Nevertheless, pristine graphene manufacturing technologies have tremendously evolved over the last 10 years, resulting in a material that may have a completely different biological profile. The biomedical community of graphene didn't follow up on the advancement of pristine graphene production. Scientific efforts focused instead on changing the explorations for functionalized graphene, which is still, in most cases, more costly to produce. There is an unmet need for knowledge about last-generation pristine graphene biocompatibility. To meet this need, in this study, we compared the impact of water-dispersed, pristine graphene prepared according to state-of-the-art techniques produced at the Cambridge Graphene Center (UK) to graphene oxide, the most widely studied GBMs for health applications.[5,19,20] The GO used in this study, prepared at Okayama University (Japan), was endotoxin-free and highly stable in water.

Moreover, most previous biocompatibility studies on graphene or GO were carried out in mice or rats and were generally focused on their toxicity toward the lungs, liver, kidney, and spleen.[21–26] However, rodents do not accurately represent humans' anatomical and physiological characteristics. Therefore, the exploitation of GBMs for biomedical applications also requires the assessment of their tolerance in large animal models closer to the human condition. Based on a prediction analysis of 2366 drugs in preclinical testing, rat, mouse, and rabbit models were shown to be highly inconsistent predictors of toxic responses in humans, with average predictive values close to 55%,[27] suggesting that we need better animal models to mimic a human physiological condition. For this reason, to facilitate the clinical translation of GBMs, we reconsidered pristine graphene and carried out an ex vivo and in vivo pilot study using swine (Sus scrofa) as a model. Indeed, the porcine model has unique anatomical similarities to humans, particularly in the cardiovascular, urinary, integumentary, and digestive systems.[28] Pig skin is the most similar to human skin, and swine is routinely used in dermatological studies. Due to the similarities between the digestive and urinary systems of humans and swine, the porcine model is used in endoscopic and laparoscopic surgery, liver or kidney transplantation, biliary or ureteral stents, and other applications.[28] Most importantly, there are many similarities to humans in anatomy and functions of the immune system, for example, the presence of tonsils, which are absent in rodents.[29] Thanks to the broad anatomical, physiological, and immunological analogies with humans, pigs have replaced dogs or monkeys over the last years as non-rodent species in pre-clinical toxicologic testing of pharmaceuticals, biopharmaceuticals, or other chemicals.[28,29] Pigs have also been used in pre-clinical evaluation of vaccine candidates and therapeutics[30,31] and nanomedicine-based studies.[32–38] As an example, in carbon-based material research, we have used this species to investigate the potential use of functionalized multi-walled carbon nanotubes as ultrasound contrasting agents due to the wide similarities of the swine and human urinary systems.[39]

In this study, GBMs were injected using an intraperitoneal (i.p.) injection route. This route has been widely used for toxicity testing, thanks to the fast absorption of injected materials.[40] In addition, this route is frequently used in cancer treatment because it can enhance tumor penetration of drugs and reduce their systemic toxic effects.[40]

In this study, by using the large-scale animal model of swine, we first evaluated the impact of two GBMs ex vivo, analyzing their interaction with different blood cells, then in vivo, using an intraperitoneal (i.p.) injection route. The porcine model was here applied as a close-to-human preclinical model for the toxicological assessment of GBMs, water-dispersible last-generation pristine graphene, and graphene oxide by a wide variety of

G. Peng, B. Fadeel
Institute of Environmental Medicine
Karolinska Institutet
Stockholm 17177, Sweden
N. D. Q. Chau, A. Bianco
CNRS
Immunology
Immunopathology and Therapeutic Chemistry
UPR 3572
University of Strasbourg ISIS
Strasbourg 67000, France
A. De la Cadena, D. Polli, G. Cerullo
Dipartimento di Fisica
Politecnico di Milano
Milan 20133, Italy
R. Vanna, D. Polli, G. Cerullo
Istituto di Fotonica e Nanotecnologie – CNR
Milan 20133, Italy
Y. A. Samad, T. Ahmed, J. Marcellino, A. Ferrari
Cambridge Graphene Centre
University of Cambridge
Cambridge CB3 0FA, UK
Y. A. Samad
Department of Aerospace Engineering
Khalifa University of Science & Technology
Abu Dhabi 127788, UAE
L. Giro, L. G. Delogu
ImmuneNano Laboratory
Department of Biomedical Sciences
University of Padua
Padua 35131, Italy
A. Ylmazer
Department of Biomedical Engineering
Ankara University
Ankara 06830, Turkey
Y. Nishina
Graduate School of Natural Science and Technology
Okayama University
Tsushimanaka, Kita-ku, Okayama 700–8530, Japan
Y. Nishina
Research Core for Interdisciplinary Sciences
Okayama University
Tsushimanaka, Kita-ku, Okayama 700–8530, Japan
L. G. Delogu
Department of Biological Sciences
Khalifa University of Science and Technology
Abu Dhabi 127788, UAE
E-mail: luciagemma.delogu@unipd.it

© 2024 The Author(s). Advanced Healthcare Materials published by Wiley-VCH GmbH

21922659, 0, Downloaded from https://onlinelibrary.wiley.com/doi/10.1002/adhm.202401783 by Cnr Roma, Wiley Online Library on [04/02/2025]. See the Terms and Conditions (https://onlinelibrary.wiley.com/terms-and-conditions) on Wiley Online Library for rules of use; OA articles are governed by the applicable Creative Commons License

approaches and multiple advanced imaging techniques. The information generated in this study is a compendium of knowledge of crucial importance for the future exploitation of these materials, including our pristine graphene, in clinical applications.

2. Results

2.1. Overview of the Study Design: From Ex Vivo to Integrative In Vivo Analysis

In our pilot study, we aimed to investigate the toxicological and immunological effects of two types of graphene-based materials (GBMs): pristine graphene (GR) and graphene oxide (GO). We thoroughly characterized the materials and assessed their potential endotoxin content and sterility, as shown in **Figure 1**. To evaluate these effects, we employed pigs as animal models, considering their suitability as an excellent human-like model. Initially, our study involved ex vivo experiments using whole blood, peripheral blood mononuclear cells (PBMCs), and macrophages. We conducted assays to evaluate hemocompatibility, viability, cellular blood count, and cytokines in these samples. Moving to in vivo experiments, we divided thirteen 12-week-old pigs into three groups. The pigs received intraperitoneal injections of either GR or GO. Blood and serum samples were collected at specific time points, including 24 h, 7, 14, and 21 days, allowing us to evaluate the toxicity and immunomodulatory effects using a comprehensive analytical approach. In our assessment, we examined the biochemical profile of globulin levels and profiled 84 immune genes. Furthermore, we analyzed the expression of immune activation markers on six different cell types and measured cytokine release. Additionally, we harvested selected organs after 21 days for histopathological analysis, aiming to gain further insights into the effects of GBMs. To specifically localize GBMs within representative organs, we utilized transient absorption imaging and Raman mapping techniques. (Figure 1).

2.2. GR and GO Synthesis and Characterization

For this study, we have prepared GR and GO with similar lateral sizes using different protocols starting from graphite. While pristine graphene was exfoliated in FBS, GO was obtained via the well-established and widely applied Hummers' method. GR and GO were characterized by SEM, AFM, Raman, and XPS. The analyses confirmed the formation of single- or few-layer nanosheets with an average lateral size of ≈0.6 µm, highly stable in the physiological environment (Figures S1 and S2, Supporting Information). The most striking differences concern the presence of defects and the level of oxygenated functions in these two materials. Raman spectra show the typical D, G, and 2D bands at ≈1350, 1580, and 2700 cm^{-1}, respectively. XPS analysis evidenced that GO is characterized by a C/O ratio of 2.2.

The endotoxin content and the sterility of GR and GO were then evaluated before ex vivo and in vivo experiments. Endotoxin content was evaluated using the TNF-α expression test (TET).[41] The cytotoxicity of GR and GO on human-monocyte-derived macrophages (HMDMs) was first evaluated by exposing the cells to GR or GO at concentrations of 5, 25, 50, and 75 µg mL^{-1} for 24 h. As shown in Figure S3A, Supporting Information, no significant cytotoxicity was observed upon exposure. HMDMs were then incubated with GR and GO at the non-toxic dose of 25 µg mL^{-1} in the presence or absence of the specific LPS inhibitor, polymyxin B sulfate (polyB) (10 µM), for 24 h. TNF-α concentration was quantified, and the presence of polyB significantly blocked the LPS-triggered TNF-α production (Figure S3A, Supporting Information). The presence of polyB did not decrease the TNF-α production triggered by GO, and GR-treated cells induced negligible TNF-α production, suggesting that both GO and GR were endotoxin-free. Sterility test was also performed by plating GR and GO suspensions on LB agar plates and incubating them overnight at 37 °C. No bacterial colonies were formed after incubation (Figure S3B, Supporting Information).

2.3. Ex Vivo Assessment of the Impact of GR and GO on Immune Cells

The impact of nanomaterials on the immune system is of critical importance.[1,8,53] As a first step, we compared the toxicity and immunomodulatory properties of GR and GO ex vivo. Hemocompatibility was first assessed. Hemolytic activity was investigated by assessing hemoglobin release after exposure of swine RBCs to increasing GR or GO concentrations (5, 25, 50, and 75 µg mL^{-1}) for 24 h. Untreated RBCs and cells treatment with distilled deionized water were used as negative and positive controls, respectively. As shown in Figure S4, Supporting Information, both GR and GO did not induce statistically significant hemolytic activities toward RBCs at any concentration tested, with the exception of GO at the highest concentration (75 µg mL^{-1}) (Figure S4, Supporting Information). Moreover, whole blood was incubated for 24 h with 50 µg mL^{-1} of GR or GO, and then changes in several blood parameters (e.g., number of platelets, red blood cells, white blood cells, hematocrit, amount of hemoglobin, mean corpuscular hemoglobin and its concentration, red blood cell distribution width and hemoglobin distribution width) were monitored. Complete blood count analyses did not show differences between GBM-treated and untreated samples (**Figure 2A**).

The impact of these GBMs on swine PBMC viability was then investigated. The cells were exposed to 50 µg mL^{-1} of GR or GO, and 24 h later, LDH levels in culture supernatants were quantified using a cytotoxicity assay. A lysis solution provided by the manufacturer and untreated PBMCs were used as positive and negative controls, respectively. Both GBMs had no appreciable impact on swine PBMC viability (Figure 2B). Next, the immune-functional impact on swine PBMCs was assessed. Cells were treated with 50 µg mL^{-1} of either GR or GO for 24 h. LPS (2 mg mL^{-1}) was used as positive control. Multiplex ELISA on PBMC supernatants revealed the release of several pro-inflammatory cytokines IL-1β, IL-6, and IL-12 in response to both GBMs, with GO having less impact on the secretion of IL-1β. Small amounts of IL-10 (0.05–0.1 ng mL^{-1}) were also detected in the supernatant of PBMCs exposed to GR, but without statistical significance (Figure 2C). Multiplex ELISA data confirmed graphene oxide-known proinflammatory potential.[7,9,54,55] No statistical difference was observed between compounds. The macrophages are phagocytic cells at the frontline of defense against foreign invaders.[56] We, therefore, analyzed the impact of GO and GR on the viability of

© 2024 The Author(s). Advanced Healthcare Materials published by Wiley-VCH GmbH

21922659, 0, Downloaded from https://onlinelibrary.wiley.com/doi/10.1002/adhm.202401783 by Cnr Roma, Wiley Online Library on [04/02/2025]. See the Terms and Conditions (https://onlinelibrary.wiley.com/terms-and-conditions) on Wiley Online Library for rules of use; OA articles are governed by the applicable Creative Commons License

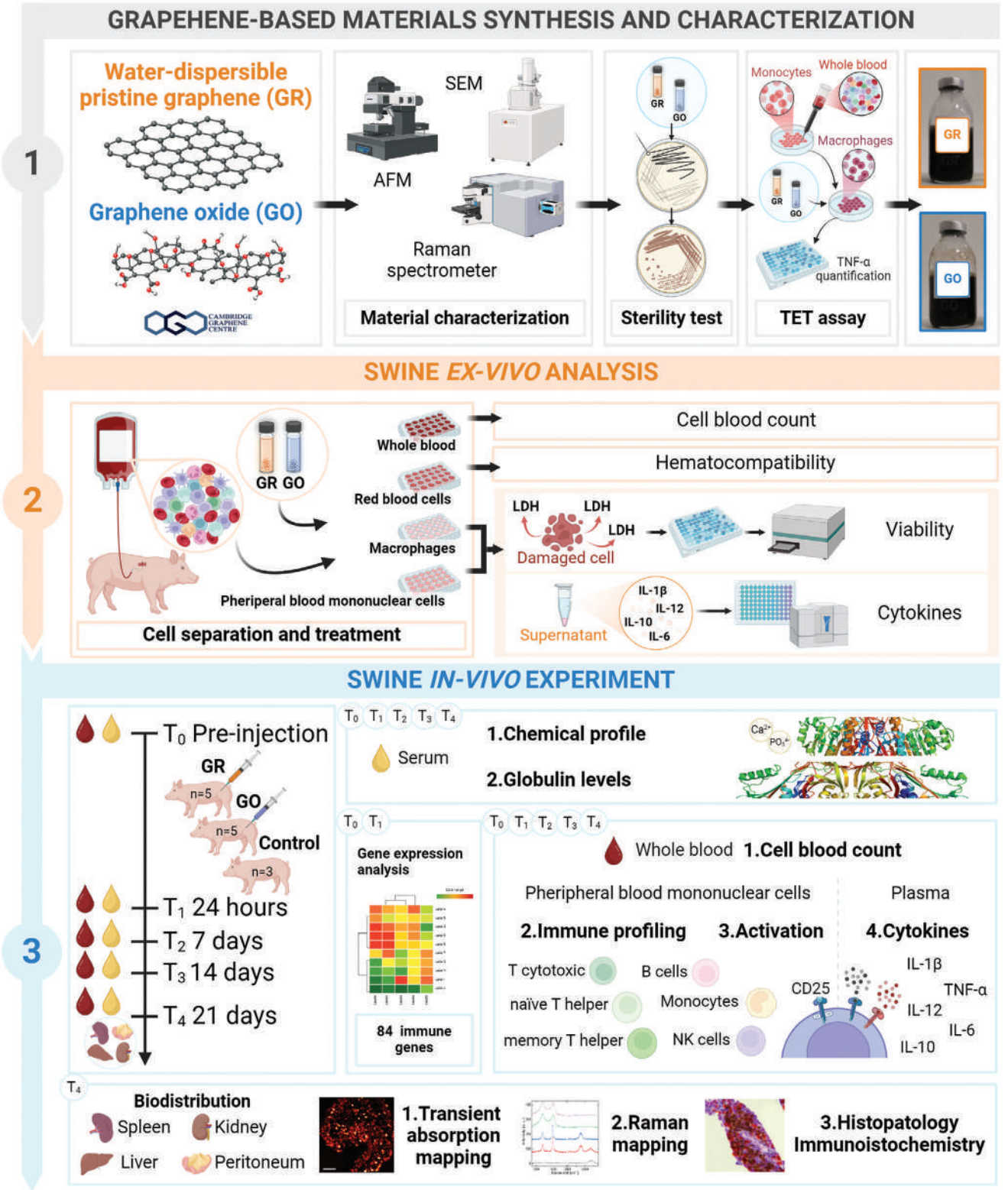

Figure 1. Study design. The present study comprehensively addressed the impact of GO versus GR, spanning from ex vivo analysis of peripheral blood cells to in vivo investigations.

© 2024 The Author(s). Advanced Healthcare Materials published by Wiley-VCH GmbH

21922659, 0, Downloaded from https://onlinelibrary.wiley.com/doi/10.1002/adhm.202401783 by Cnr Roma, Wiley Online Library on [04/02/2025]. See the Terms and Conditions (https://onlinelibrary.wiley.com/terms-and-conditions) on Wiley Online Library for rules of use; OA articles are governed by the applicable Creative Commons License

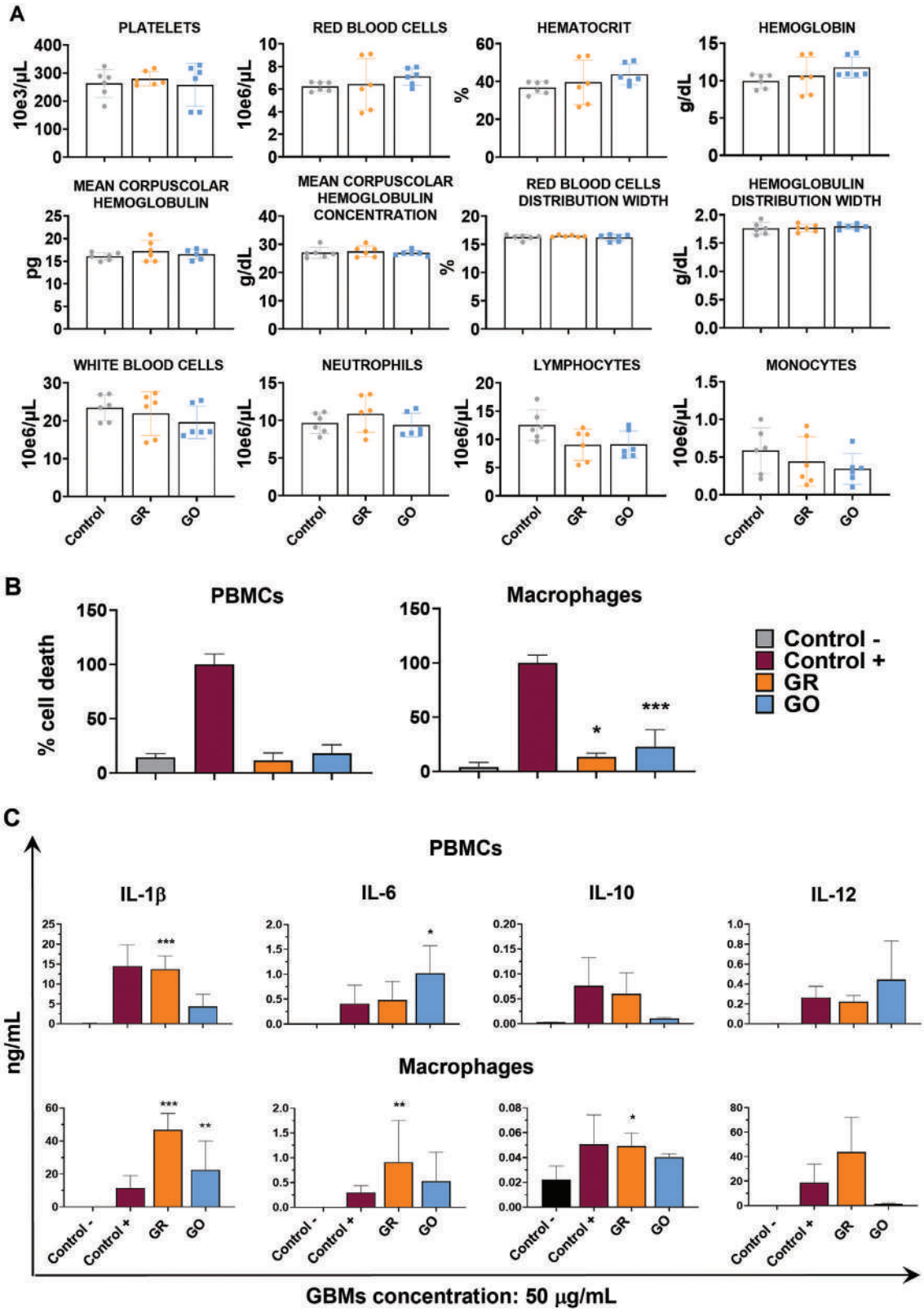

Figure 2. GMBs impact on ex vivo pig blood cells. A) Changes in swine whole blood after GR or GO. Whole blood was harvested from three healthy swine and was incubated with 50 µg mL^{-1} of GR or GO or left untreated (control). After 24 h, complete blood counts were performed. Changes in the number of red blood cells (RBC), platelets (PLT), and total white blood cells (WBC), then divided into neutrophils (NEUTR), lymphocytes (LYMPH), and monocytes (MONO), were analyzed. Changes in hematocrit (HCT), amount of hemoglobin (HGB), mean corpuscular volume (MCV), mean corpuscular hemoglobin

© 2024 The Author(s). Advanced Healthcare Materials published by Wiley-VCH GmbH

21922659, 0, Downloaded from https://onlinelibrary.wiley.com/doi/10.1002/adhm.202401783 by Cnr Roma, Wiley Online Library on [04/02/2025]. See the Terms and Conditions (https://onlinelibrary.wiley.com/terms-and-conditions) on Wiley Online Library for rules of use; OA articles are governed by the applicable Creative Commons License

macrophages and on the ability of these cells to release cytokines. Both GBMs induced a statistically significant reduction in swine macrophage viability and triggered sustained release of cytokines IL-1β, IL-6, and IL-12 (Figure 2B,C). Differences between GBMs were observed, with GO inducing lower release of both IL-1β and IL-12 than GR (Figure 2C).

2.4. In Vivo Systemic and Immunological Impact of GR and GO in Swine

In this pilot study, GBM suspensions were administered intraperitoneally in pigs. Fifteen mg (0.5 mg Kg^{-1}) of either GR or GO were injected in 12-week-old pigs of ≈30 kg of weight. In Table S1, Supporting Information, we report the animal group's random selection for the different treatments. The used concentration (corresponding to 6.8 mg m^{-2},[28]) was similar to other studies on GBM toxicity in mice, where concentrations ranging from 1 to 20 mg Kg^{-1} (corresponding to 3–60 mg m^{-2}) were administered intravenously or intraperitoneally into animals.[17,25,26,57–59] During the administration, clinical observations were performed; electrocardiogram, body temperature, oxygen saturation, blood pressure, and respiratory rate were monitored by a portable multi-parameter veterinary monitor. The vital parameters were tracked until awakening (almost 15 min post-injection), and no alterations were observed (data not shown). Clinical examinations were performed daily by trained veterinarians for up to 21 days. No general signs of toxicity (e.g., seizures, respiratory, gastrointestinal, or neurological symptoms) or reduced growth were observed throughout the study, and the experiments concluded with a 100% survival rate. No differences between males and females were observed.

To obtain a deeper understanding of the impact of GR or GO on circulating PBMCs early after injection, the relative expression of 84 genes related to common cytokines (Table S3, Supporting Information) was evaluated in three representative pigs per group at T_0 and T_1 (24 h post-injection) (**Figures 3** and S5, Supporting Information). Importantly, non-supervised hierarchical clustering analysis shows that the gene expression patterns were similar between GR- and GO-groups and the gene expression profile in T_1 was separated from T_0. Gene expression at T_1 in each group was first normalized to the same individuals at T_0 and shown as volcano plots. In the control group (**Figure 4A**), five genes were significantly up-regulated compared to T_0, and three of them demonstrated at least a twofold difference (*ADIPOQ, TXLNA, THPO*). As shown in Figure 4A, two genes were significantly different in the GR-group compared to the control: *IL1A* (upregulated) and *FASLG* (downregulated). In comparison, five genes were significantly upregulated in the GO-group compared to the control group: *IL21, BMP2, AIMP1, LTB*, and *IL16*; and *ADIPOQ* was significantly downregulated. Differences in ADIPOQ might not be linked to GBM treatment since ADIPOQ gene expression was upregulated also in the control group (T_1 compared to T_0). A summary of the fold regulation and the *p* values of statistically different expressed genes between treated and untreated pigs is shown in Table S5, Supporting Information. In the GR-group (Figure 4B), four genes were significantly upregulated, and two genes were significantly downregulated. In comparison, 16 genes were significantly upregulated in the GO-group, and one gene was downregulated (Figure 4B).

To further minimize the effects of variation among individuals, we grouped the nine individuals at T_0 and evaluated the gene expression profile in each group at T_1 (Figure S5, Supporting Information). In this case, when we excluded the significant changes of genes observed in the control group, there were 6 genes significantly upregulated in the GR-group (INHBA, IL17B, IL4, TGFB2, LTB, LOC100621682), 4 genes significantly upregulated in GO group (LTA, LTB, IL16, BMP1), and 2 genes significantly downregulated in GO-group (IL27, BMP5). The fold regulation and the *p*-value of statistically differently expressed genes are listed in Table S4, Supporting Information. The results are presented as the average of three individuals in each group, and a *p*-value less than 0.05 was considered statistically significant.

A total of 28 hematological and biochemical parameters were collected at different time points post-injection during in vivo experimentation for comprehensive toxicity analysis (**Figure 5**). Blood samples were collected at T_0 (pre-injection), 1 (T_1), 7 (T_2), 14 (T_3), and 21 (T_4) days post-injection from the 13 animals. Impact of GBMs on different whole blood components was monitored through complete blood count (RBC parameters, platelets and white blood cells (WBC) counts, and WBC differential counts) (Figure 5A). We observed fluctuations in some RBC parameters (RBCs, hemoglobin, hematocrit levels) in pigs treated with either GO or GR at T_1 and T_2, nevertheless, no statistically significant differences were observed between GBMs-treated groups compared to controls. In addition, these three parameters returned to baseline levels in all tested subjects by the end of the study in all subjects. Overall, no statistically significant differences between groups (evaluated with Bonferroni correction) were detected in all RBC parameters at any time point (Figure 5A), indicating that GBMs did not induce anemia or hemolysis. Platelet readings presented large fluctuations in all pigs. Particularly, test subjects #04 (GO-group) and #08 (GR-group) presented extremely low platelet count at T_1, nevertheless, levels returned to normal before the end of the experiment, and no statistically significant differences were observed between groups during the study (Figure 5A). Moreover, no statistically significant differences were observed in the WBC total count and WBC differential count. Overall, the data indicated the absence of

(MCH) and its concentration (MCHC), red blood cell distribution width (RDW) and hemoglobin distribution width (HDW) were also monitored. Data from three different pigs are presented as mean and SD. Values of graphene-treated samples were compared to the corresponding untreated control (Control) using a one-way ANOVA followed by Bonferroni's multiple comparison test. B, C) GR and GO impact on PBMCs and macrophages. Cells were left untreated (Control) or stimulated with 50 mg mL^{-1} of GR or GO. B) 24 h post-exposure cell viability was assessed using a non-radioactive cytotoxic assay. A lysis solution provided by the manufacturer was used as a positive control. C) 24 h post-exposure cytokines (IL-1β, IL-6, IL-10, IL-12) levels in culture supernatants were determined using a multiplex ELISA. LPS (2 µg mL^{-1}) was used as a positive control (Control +). Mean data and SD from three independent experiments using different animals are shown. Values of GBMs-treated samples were compared to the corresponding untreated control (Control -) using a one-way ANOVA followed by Bonferroni's multiple comparison test. ***$p < 0.001$, **$p < 0.01$.

© 2024 The Author(s). Advanced Healthcare Materials published by Wiley-VCH GmbH

21922659, 0, Downloaded from https://onlinelibrary.wiley.com/doi/10.1002/adhm.202401783 by Cnr Roma, Wiley Online Library on [04/02/2025]. See the Terms and Conditions (https://onlinelibrary.wiley.com/terms-and-conditions) on Wiley Online Library for rules of use; OA articles are governed by the applicable Creative Commons License

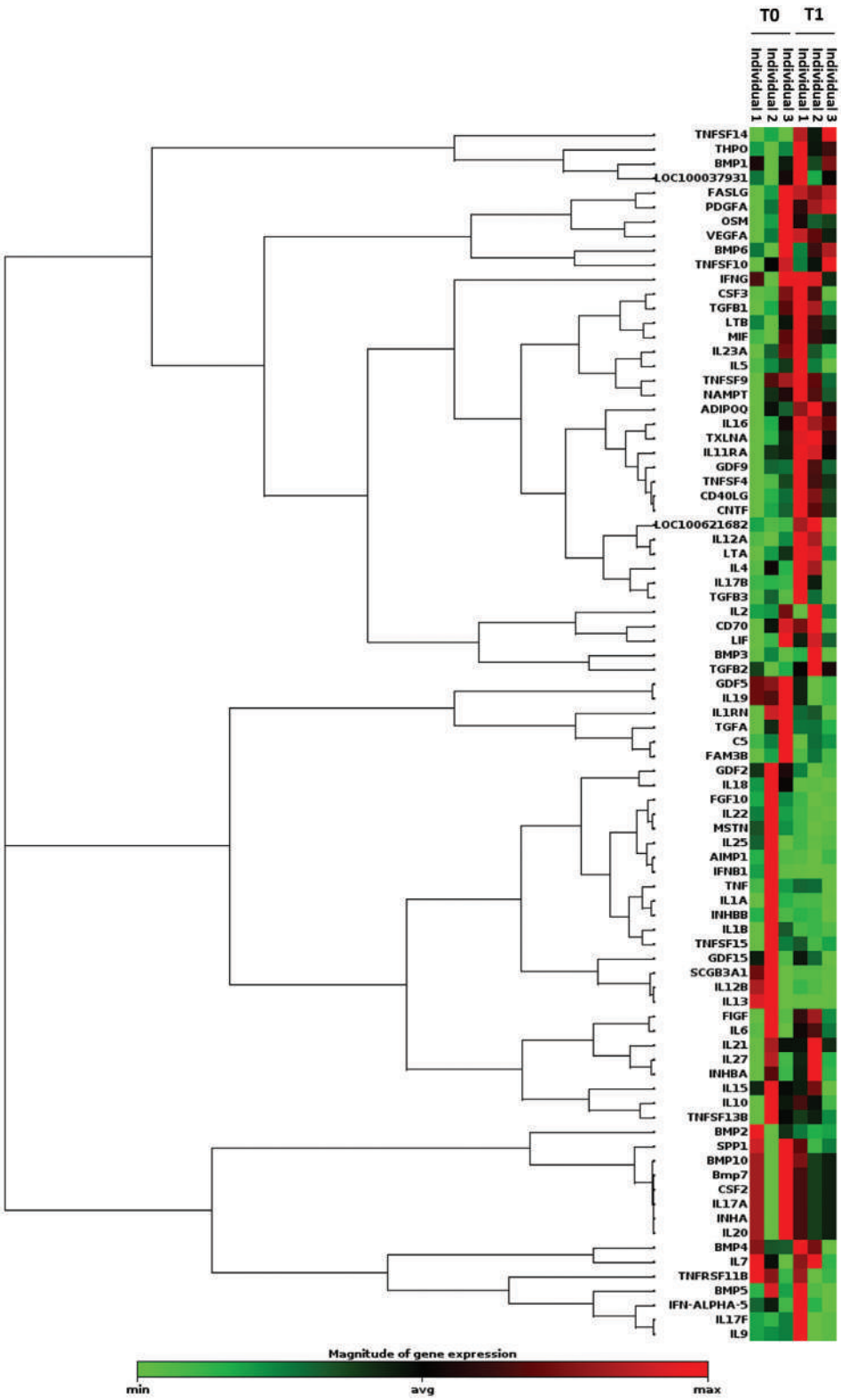

Figure 3. Modulation of 84 genes in PBMCs after GR or GO injection. Pigs were injected intraperitoneally with 15 mg of GR or GO or water, all with glucose (final glucose 5% w/v). Pre-injection (T_0) and after 24 h (T_1), PBMCs were purified from EDTA blood. Gene expression was carried out on three pigs per group. T_0 was presented as the average of nine individuals. Non-supervised hierarchical clustering analysis of 84 gene expression patterns across the groups. The colors in the cells represent the relative magnitude of gene expression. The black color represents the average magnitude of gene expression. The brightest green represents the smallest value, and the brightest red represents the highest value.

© 2024 The Author(s). Advanced Healthcare Materials published by Wiley-VCH GmbH

21922659, 0, Downloaded from https://onlinelibrary.wiley.com/doi/10.1002/adhm.202401783 by Cnr Roma, Wiley Online Library on [04/02/2025]. See the Terms and Conditions (https://onlinelibrary.wiley.com/terms-and-conditions) on Wiley Online Library for rules of use; OA articles are governed by the applicable Creative Commons License

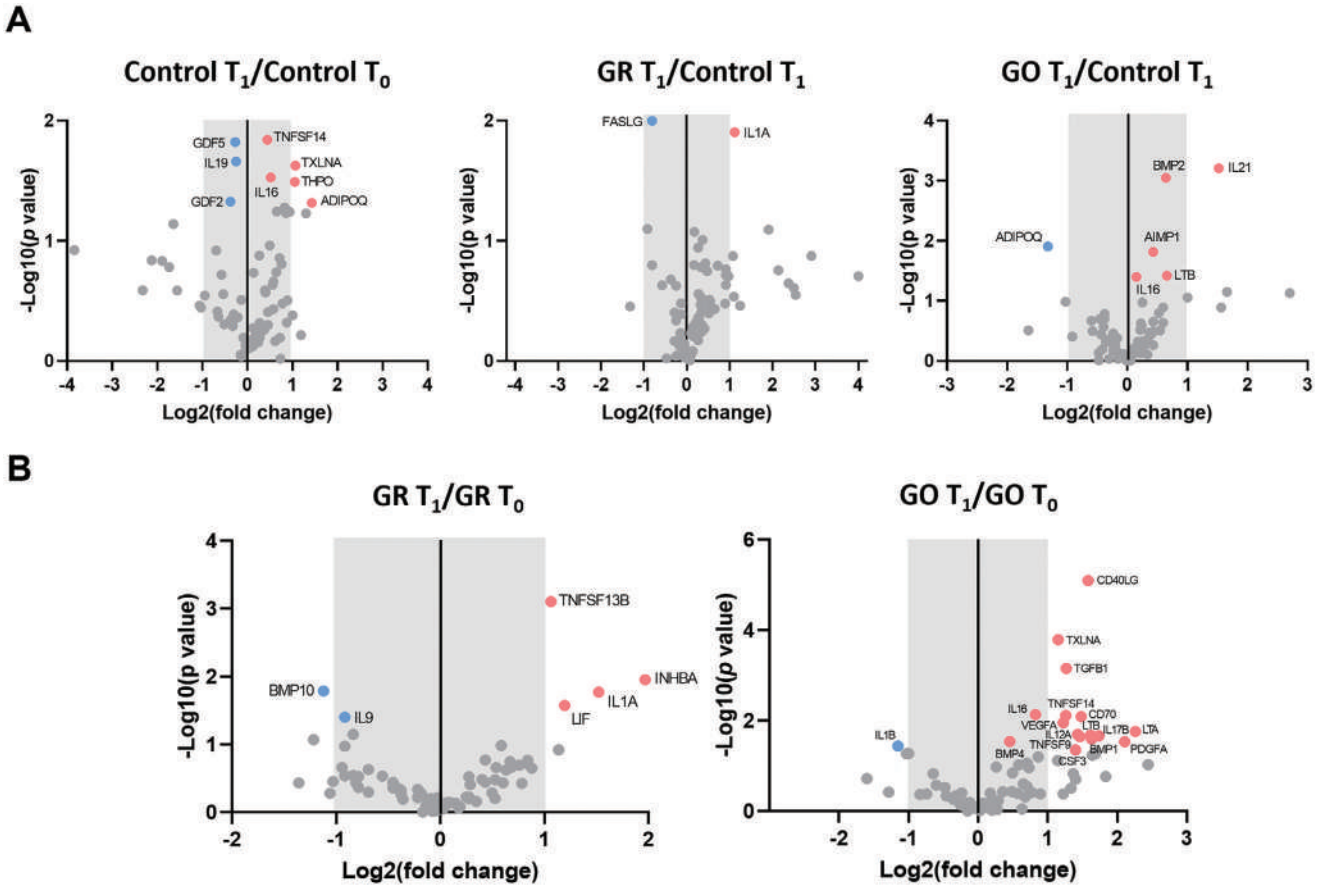

Figure 4. Changes in PBMCs gene expression in pigs after GR or GO injection. Pigs were injected intraperitoneally with 15 mg of GR or GO alongside controls. Pre-injection (T_0) and after 24 h (T_1), PBMCs were purified from EDTA blood. Gene expression was carried out on three pigs per group. In Panel A, three volcano plots show the 84 genes expression at T_0 in control, T_1 in control, GR, and GO groups. In Panel B, two volcano plots show the 84 genes expression at T_1 in GR and GO groups compared to T_0 within the groups, for both A and B, significantly up- and down-regulated genes were marked in red and blue, respectively. Genes plotted farther from the central axis have larger changes in gene expression. Thresholds of twofold change were indicated in the shadow. The statistically significant difference was set as $p < 0.05$.

inflammatory or toxic response in the test subjects treated with both GBMs.

To have a full view of immune subpopulations, PBMCs were isolated and investigated by flow cytometry using several clusters of differentiation markers (Figure S7, Supporting Information). Neither GR nor GO altered the proportion of lymphocyte subsets. Hence, no differences between groups were observed between the percentage of B cells, NK cells, T cells, or different T cell subpopulations (cytotoxic ($CD3^+CD8^{high}CD4^-$), naïve T helper ($CD3^+CD8^-CD4^+$), memory T helper ($CD3^+CD8^{low}CD4^+$)) (Figure S8, Supporting Information).

A wide variety of serum markers were monitored to evaluate liver functions.[60] Serum aspartate aminotransferase (AST) and alkaline phosphatase (ALP) levels reflect hepatocyte health and function, whereas serum bilirubin, triglycerides, and cholesterol parameters depict the liver's metabolic capacity. Normal gamma-glutamyl transpeptidase (GGT) levels reflect the health of the biliary tract. For all these parameters, no apparent abnormalities were observed outside normal physiological fluctuation. Only an escalation trend for ALP levels was observed in the GO-group, although without statistical significance (Figure 5B). Collectively, no statistically significant difference between groups was observed, and overall, our results indicated that both GR and GO do not cause liver damage or functional impairment. In addition, as displayed in Figure 5B,C, no decreases in total protein or albumin levels were observed. The standard panel for renal function assessment included serum urea and creatinine levels alongside serum electrolytes (sodium and potassium) measurement. Both urea and creatinine levels were unaffected in all groups during the study, indicating that both GBMs did not impair renal filtration functions. Furthermore, sodium and potassium levels remained within the normal range for the study, suggesting that these GBMs did not affect the kidney's ability to maintain electrolyte balance (Figure 5B). The absence of renal or liver dysfunctions was also confirmed by electrophoretic results, which revealed no differences between the groups in terms of number or proportion of serum globulins (Figure 5C). Electrophoretic data also highlighted the absence of inflammatory status: both GR and GO do not cause an increase in the proportion of $\alpha 1$ globulin compared to albumin (Figure 5C). Finally, creatine phosphokinase (CPK) levels were monitored overtime. Levels of

© 2024 The Author(s). Advanced Healthcare Materials published by Wiley-VCH GmbH

21922659, 0, Downloaded from https://onlinelibrary.wiley.com/doi/10.1002/adhm.202401783 by Cnr Roma, Wiley Online Library on [04/02/2025]. See the Terms and Conditions (https://onlinelibrary.wiley.com/terms-and-conditions) on Wiley Online Library for rules of use; OA articles are governed by the applicable Creative Commons License

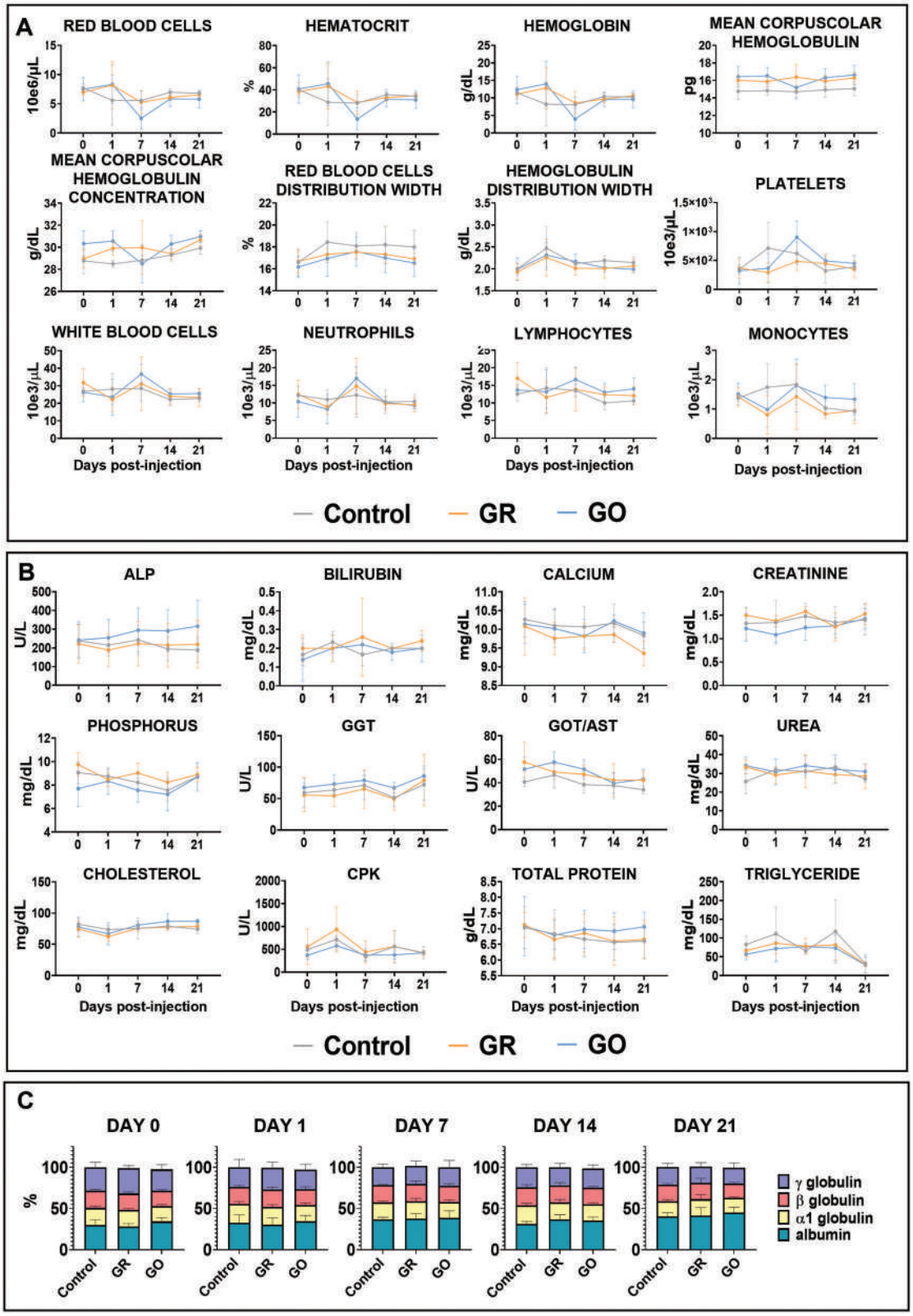

Figure 5. Hematological and biochemical profile of pigs treated with GR or GO. Pigs were injected intra-peritoneally with 15 mg of GR or GO alongside controls. Pre-injection (0) and after 1, 7, 14, and 21 days, blood was collected to perform a complete blood count biochemical and electrophoretic profile. A) Hemocompatibility. Changes in the number of red blood cells, hematocrit, amount of hemoglobin, mean corpuscular hemoglobin and its concentration, red blood cell distribution width and hemoglobin distribution width, and platelets number were monitored. Changes in the number of white blood

© 2024 The Author(s). Advanced Healthcare Materials published by Wiley-VCH GmbH

21922659, 0, Downloaded from https://onlinelibrary.wiley.com/doi/10.1002/adhm.202401783 by Cnr Roma, Wiley Online Library on [04/02/2025]. See the Terms and Conditions (https://onlinelibrary.wiley.com/terms-and-conditions) on Wiley Online Library for rules of use; OA articles are governed by the applicable Creative Commons License

this enzyme, also known as creatine kinase, are regarded as an indicator of cardiac function, and their rise was observed in both mice and non-human primates undergoing adverse reactions to GBMs.[53] In our study, no differences between the groups were observed at any tested time point (Figure 5B). Overall, our results from the hematological, biochemical, and electrophoretic analyses indicated that both GR and GO were well tolerated by all animals in the treatment groups.

Potential immuno-modulatory properties of the GBMs were also investigated. Expression of a key cell activation marker (CD25 expression) of circulating PBMCs and cytokine plasma levels were monitored over time until 21 days post-injection. No upregulation of CD25 on either monocytes, B cells, T cells, or NK cells was detected at any time post-injection (**Figure 6**). Plasma levels of IL-1β, IL-2, IL-4, IL-6, IL-10, IL-12, and TNF-α were also assessed over the study, and our results show that neither GR nor GO administration increased circulating levels of any of these cytokines (Figure 6). TNF-α values were below the detection levels of the kit (data not shown). No alteration in plasma levels of pro-inflammatory cytokines (in particular IL-1β, IL-6, TNF-α) also indicated the absence of inflammatory response in the test subjects treated with both GBMs.

2.5. Biodistribution of GR and GO and its Impact on Vital Organs in Swine

The animals were sacrificed at the end of the experiment (21 days post-injection) in accordance with the rules of animal welfare, and necroscopies were performed. No gross pathological lesions were found at necroscopy, but numerous randomly scattered spherical or oblong-shaped aggregates were observed in the peritoneum of the GO-treated group (Figure S9A, Supporting Information). GO aggregates presented variable dimensions. Some of the most prominent aggregates (up to 30 mm in diameter or length) are presented in Figure S9B, Supporting Information (representative images of tested subjects #04, #06), but smaller spherical aggregates (average 1 mm) were observed in different parts of the mesentery of all the GO-treated pigs (Figure S9A, Supporting Information)(representative images of tested subjects #02, #07, #14). No GR aggregates were instead visible to the naked eye (Figure S9A, Supporting Information). Histological examinations revealed aggregates of nanomaterials in the peritoneum in both treated pigs, with GR aggregates presenting an average diameter lower than 0.2 mm. Neither GR nor GO clusters were visible in the parenchyma of the liver or spleen, and H&E staining did not reveal any sign of necrosis, inflammation, atrophy/hypertrophy, or other alterations in these organs (Figure S10, Supporting Information). Previous studies in mice reported that GO or PEGylated GO derivatives injected i.p. were accumulated in cells of the reticuloendothelial system (RES) in either liver or spleen.[19,25] Nevertheless, in the present study, we found no evidence of accumulation of either GO or GR in these organs. On the contrary, aggregates of GO were observed in the serosa of the liver and spleen (Figure S11, Supporting Information). After entering the vascular system, nanomaterials could pass through the kidneys and be excreted through urine. We thus evaluated whether GR or GO induced glomerular alteration or induced other damages in the kidneys. H&E did not reveal any evidence of atrophy, hypertrophy, necrosis, inflammation, vacuolation, tubular dilatation, or any other sign of illness in these organs (Figure S10, Supporting Information).

To further ascertain the presence of the two GBMs in tissues, we applied two complementary approaches, transient absorption (TA) microscopy and Raman mapping, for the label-free detection of GBMs in situ. TA microscopy is a nonlinear optical technique that allows fast identification of GBMs with high spatial resolution.[61] While it cannot characterize the GMBs in terms of number of layers, doping, and defects, as in spontaneous Raman microscopy, its short pixel dwell time (»1 ms) allows scanning of large sample areas with high spatial resolution. Because TA imaging is capable of detecting graphitic species at concentrations as low as 10 μg mL^{-1},[62] it was used to investigate the presence of GR and GO in tissue samples in the current model. In brief, in TA microscopy, the sample is illuminated by two ultrashort light pulses, the pump, and the probe, and the differential transmission ($\Delta T/T$) of the probe pulse is monitored as a function of the pump/probe delay t. For our experiment, we chose pump/probe wavelengths of 1030/780 nm. In the presence of GR or GO incorporated in the tissue, an intense positive $\Delta T/T$ signal appears due to Pauli blocking of graphene's absorption following the generation of a hot carrier distribution in the conduction band by the pump pulse.[63] The $\Delta T/T$ signal decays within ≈2 ps (2000 fs) due to carrier cooling in graphene, as shown by the images acquired at different t (**Figure 7A,B**). Thus, for imaging purposes, we chose a positive delay t = 500 fs to avoid coherent artifacts, such as cross-phase modulation or stimulated Raman-scattering, which occur during the temporal overlap of pump and probe pulses, thus obtaining a $\Delta T/T$ signal specific for GR or GO. Using these parameters, TA images acquired from control and GR- and GO-treated tissue samples (Figure 7C and Figure S12, Supporting Information) showed TA signals only in the mesentery, with higher signals in GR-treated pigs (up to $\Delta T/T$ of $\approx 0.5 \times 10^{-3}$), relative to GO-treated pigs (up to $\Delta T/T$ of $\approx 0.3 \times 10^{-3}$). GR aggregates detected in mesentery had a diameter spanning from 4 to 12 μm. On the contrary, GO or GR signals were not observed in the kidney, liver, and spleen, whose corresponding TA images are comparable to those obtained from control samples (Figure 7C and Figure S12, Supporting Information).

Confocal Raman spectroscopy is a powerful tool not only to identify carbon-based materials[64–66] but also to quantify the

cells, then divided into neutrophils, lymphocytes, and monocytes, were assessed. B) Biochemical profile. Serum levels of alkaline phosphatase (ALP), bilirubin, cholesterol, calcium, creatinine, phosphorus, gamma-glutamyl transferase (GGT), aspartate transferase (GOT/AST), urea, creatine phosphokinase (CPK), total protein, and triglyceride were determined using an automated spectrophotometer. C) Electrophoretic results. Percentages of albumin, α1-globulin, β-globulin, and γ-globulin were determined through electrophoresis. For both A) and B) and C), data from three (controls) or five (treated) different pigs are presented as mean and SD. At each time post-injection, values were compared using a one-way ANOVA followed by Bonferroni's multiple comparison test.

© 2024 The Author(s). Advanced Healthcare Materials published by Wiley-VCH GmbH

21922659, 0, Downloaded from https://onlinelibrary.wiley.com/doi/10.1002/adhm.202401783 by Cnr Roma, Wiley Online Library on [04/02/2025]. See the Terms and Conditions (https://onlinelibrary.wiley.com/terms-and-conditions) on Wiley Online Library for rules of use; OA articles are governed by the applicable Creative Commons License

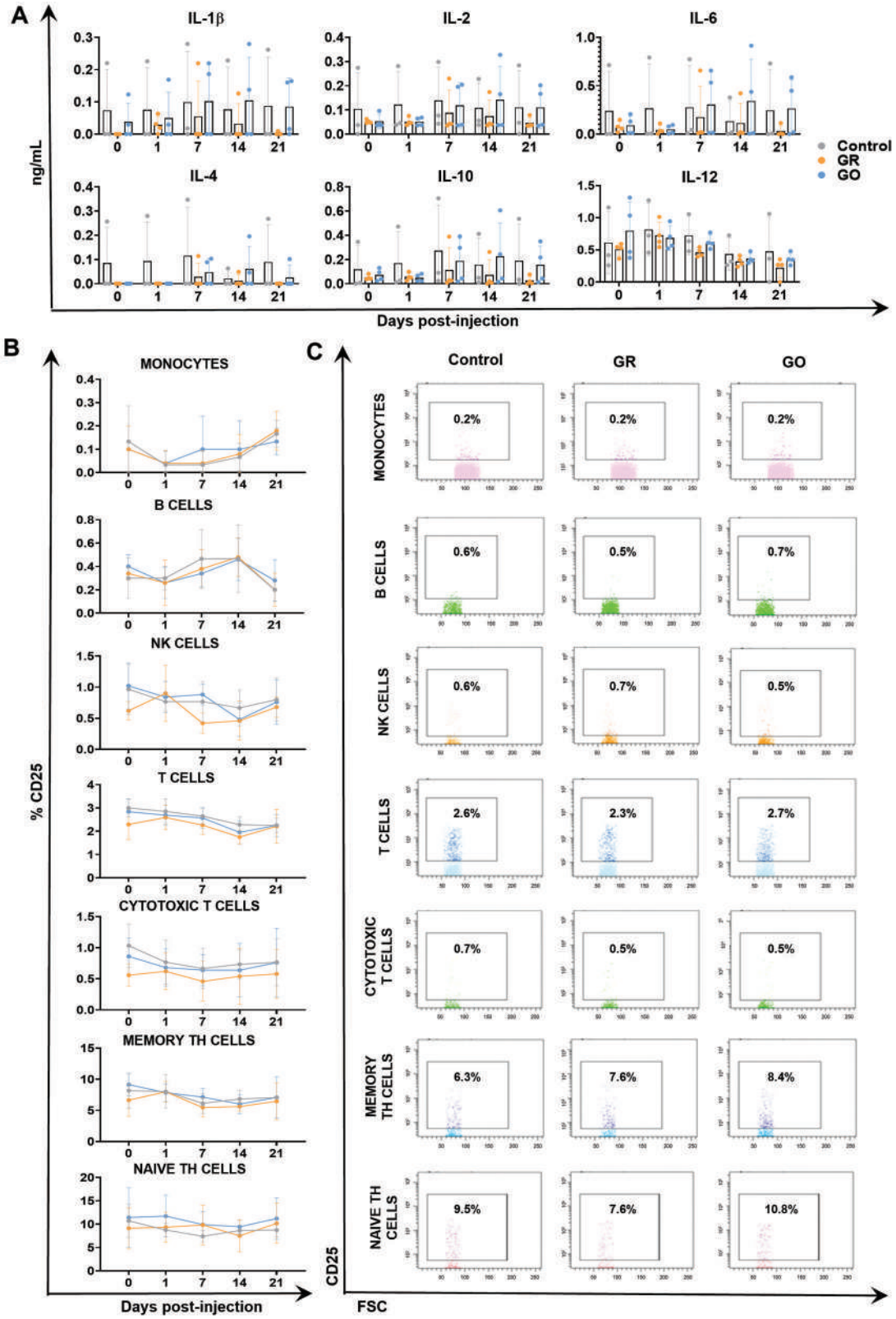

Figure 6. GR or GO administration did not affect cytokine levels or early activation marker (CD25) expression on PBMCs. Pigs were injected intraperitoneal with 15 mg of GR or GO alongside controls. Pre-injection (0) and after 1, 7, 14, and 21 days, EDTA blood was collected, PBMCs were purified, and plasma was collected. A) Plasma levels of IL-1β, IL-2, IL-4, IL-6, IL-10, and IL-12 were monitored over time using a multiplex ELISA. Data from three controls or four treated different pigs are presented as mean + SD. B) CD25 (activation marker) expression on monocytes, B cells, NK cells, and T cells,

© 2024 The Author(s). Advanced Healthcare Materials published by Wiley-VCH GmbH

21922659, 0, Downloaded from https://onlinelibrary.wiley.com/doi/10.1002/adhm.202401783 by Cnr Roma, Wiley Online Library on [04/02/2025]. See the Terms and Conditions (https://onlinelibrary.wiley.com/terms-and-conditions) on Wiley Online Library for rules of use; OA articles are governed by the applicable Creative Commons License

then subdivided into cytotoxic ($CD8^{high}CD4^{-}$), memory T helper ($CD8^{+}CD4^{+}$), naïve T helper ($CD8^{-}CD4^{+}$) was determined using flow cytometry. Data from three (controls) or five (treated) different pigs are presented as mean + SD. C) Representative dot plots are displayed. At each time post-injection, values of cytokines or activation markers were compared using a one-way ANOVA followed by Bonferroni's multiple comparison test.

presence and evolution of physical parameters like strain,[67,68] doping,[69–72] and disorder[73,74] in them. We performed confocal micro Raman spectroscopy in GR- and GO-treated tissues, control tissues, and control GR and GO samples. Four different kinds of tissues, that is, mesentery (mes), spleen, liver, and kidney, were investigated using a 514.5 nm wavelength laser. We performed Raman mapping in a 20 μm × 20 μm area of the control tissues. Representative Raman spectra from mesentery, spleen, liver, and kidney tissues are presented as black traces in **Figure** 8A–C (from two different regions) and 8D, respectively. Here we observe prominent Raman peaks at 1244,1339, 1453, 1585, 1670, 2880, and 2935 cm^{-1}. Peaks at 1244 and 1339 cm^{-1} are assigned to RNA and nucleic acids, respectively. The Raman appearing at 1453 cm^{-1} is assigned to the bending of CH_2 and CH_3 groups in cholesterol and fatty acids and C—H vibrations in proteins and lipids.[75] The peak at 1588 cm^{-1} is assigned to the bending of the C═C bond of phenylalanine and the vibration of the C═C bond of olefinic.[75] The peak at 1670 cm^{-1} is assigned to the stretching of the C═O bond coupled to the bending of the N—H bond in amide and ceramides. The peak at 2880 cm^{-1} is assigned to the stretching of the CH_2 group of lipids and proteins. The peak at 2935 cm^{-1} is assigned to C—H stretching.[75] We then investigated GR- and GO-treated tissues using Raman mapping. At least 400 Raman spectra were collected from each sample to perform statistical analysis. The representative Raman spectra from GR-treated mesentery, spleen, liver, and kidney tissues are presented as red traces in Figure 8A (Mes_GR), Figure 8B (Spleen_GR), Figure 8C (Liver_GR), and Figure 8D (Kidney_GR), respectively. The representative Raman spectra from GO-treated mesentery, spleen, liver, and kidney tissues are presented as green traces in Figure 8A (Mes_GO), Figure 8B (Spleen_GO), Figure 8C (Liver_GO), and Figure 8D (Kidney_GO), respectively. To identify the GR and GO Raman signals from these Raman spectra, we have subtracted the background Raman signal arising from the tissues. The representative background subtracted Raman signal of the GR in mesentery, spleen, liver, and kidney tissues are presented as blue traces in Figure 8A (Mes_GR –Mes), Figure 8B (Spleen_GR –Spleen), Figure 8C (Liver_GR –Liver), and 8D (Kidney_GR –Kidney), respectively. The representative background subtracted

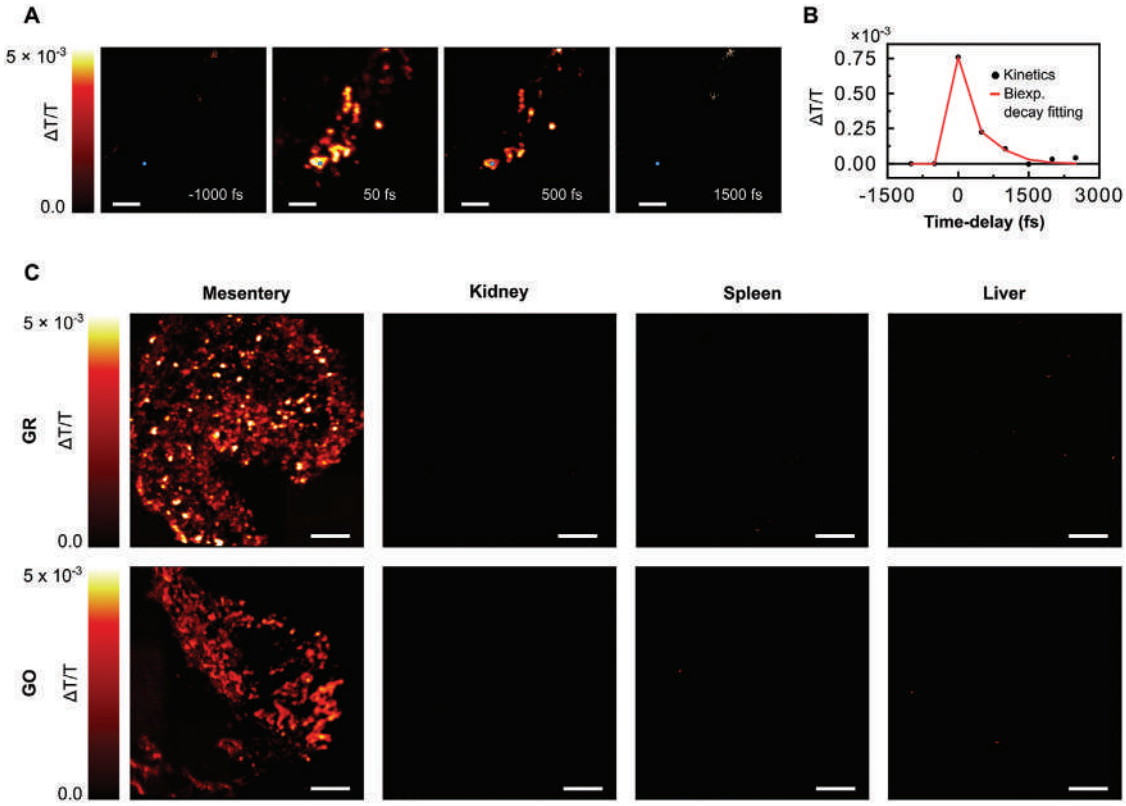

Figure 7. TA imaging experiments. Pigs were injected intra-peritoneally with 15 mg of GR or GO alongside controls and 21 days later were sacrificed. TA imaging was carried out on paraffin-embedded sections of the peritoneum, liver, spleen, and kidney collected 21 days from GR or GO injected pigs. A) TA-based detection of graphene species was demonstrated and optimized by setting different time delays of ΔI/I signal decay, extracted from TA images on mesentery from animals treated with GR; the blue dots in the TA images are those used to produce the curve in panel B. B) Time-delay curve of TA imaging. C) Representative TA images collected from tissue samples from organs extracted from animals treated with GO or GR. See Figure S12, Supporting Information for TA images related to control animals. Scale bars: 50 μm.

© 2024 The Author(s). Advanced Healthcare Materials published by Wiley-VCH GmbH

21922659, 0, Downloaded from https://onlinelibrary.wiley.com/doi/10.1002/adhm.202401783 by Cnr Roma, Wiley Online Library on [04/02/2025]. See the Terms and Conditions (https://onlinelibrary.wiley.com/terms-and-conditions) on Wiley Online Library for rules of use; OA articles are governed by the applicable Creative Commons License

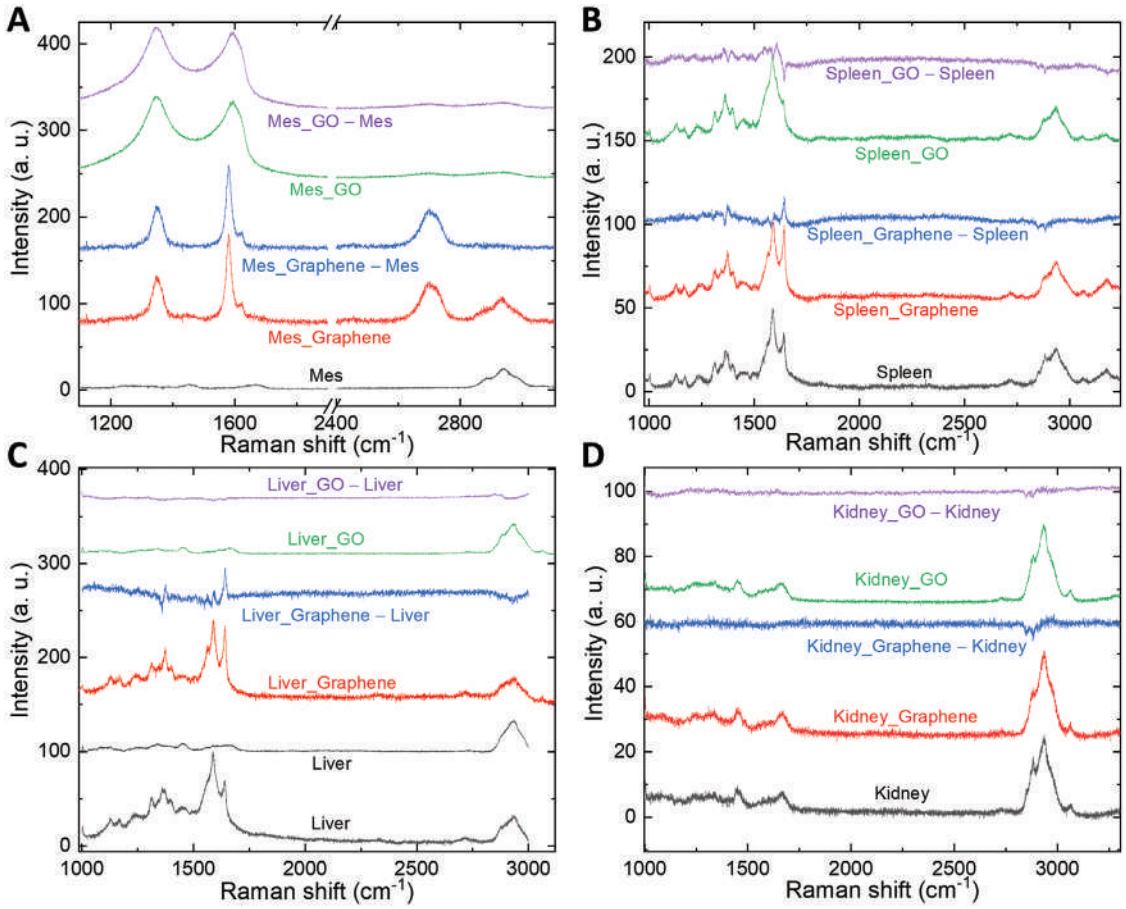

Figure 8. Representative Raman spectra from control swine tissues and graphene and GO treated swine tissues. A) The representative Raman spectra from control swine mesentery (mes), graphene treated mesentery (Mes_Graphene), and GO treated mesentery (Mes_GO) tissues are shown as black, red, and green traces, respectively. The representative Raman spectra of graphene and GO in the mesentery tissues are obtained by subtracting the mesentery Raman signal from the Mes_Graphene and Mes_GO, respectively. These data are presented as light blue (Mes_Graphene – Mes) and magenta (Mes_GO – Mes), respectively. B) The representative Raman spectra from control swine spleen, graphene treated spleen (Spleen_Graphene), and GO treated spleen (Spleen_GO) tissues are shown as black, red, and green traces, respectively. The spleen background subtracted Raman signal from the graphene and GO treated samples are presented as light blue (Spleen_Graphene – spleen) and magenta traces (Spleen_GO – spleen), respectively. C) Similarly, the representative Raman spectra from control swine liver, graphene treated liver (Liver_Graphene), and GO treated spleen (Liver_GO) tissues are shown as black (from two different regions), red and green traces, respectively. The spleen background subtracted Raman signal from the graphene and GO treated samples are presented as light blue (Liver_Graphene – Liver) and magenta traces (Liver_GO – Liver), respectively. D) Similarly, the representative Raman spectra of control swine kidney and graphene and GO treated kidney tissues are shown.

Raman signal of the GO in mesentery, spleen, liver, and kidney tissues are presented as magenta traces in Figure 8A (Mes_GO –Mes), Figure 8B (Spleen_GO –Spleen), Figure 8C (Liver_GO –Liver), and Figure 8D (Kidney_GO –Kidney), respectively.

The background-subtracted Raman spectrum (the blue trace) in Figure 8A shows strong Raman modes at the wavenumbers ≈1350, 1580, 1623, and 2700 cm^{-1}. These Raman modes can be identified as the *D, G, D's*, and the *2D* modes of graphene.[64–74] The background-subtracted Raman spectrum in magenta in Figure 8A shows strong, broad Raman modes at the wavenumbers ≈1350 and 1580 cm^{-1}. These Raman modes can be identified as the *D and G* modes of GO. It is clear from the background-subtracted spectra that GR and GO are present in the treated mesentery tissues. However, no significant GR and GO signal is detected from GR and GO-treated spleen, liver, and kidney tissues. Spatial map of the Raman shift of *G* peak (Pos(*G*)), full width at half maxima of *G* peak (FWHM(*G*)), and the ratio of intensities of *D* and *G* peaks (*I*(*D*)/*I*(*G*)), from GR- and GO-treated mesentery tissues are presented in Figures S13 and S14, Supporting Information, respectively.

We then focused our attention on understating the changes in GR and GO before and after injection into the mesentery tissues. Representative Raman spectra of GR/GO and tissue background subtracted Raman spectra of GR/GO after injection into the mesentery tissues are presented in **Figure** 9A,B as black and blue traces, respectively. Changes in the *I(D)/I(G)* visible in the Raman spectra of graphene before and after injection and changes in the G peak are observed in the Raman spectra of both GR and GO before and after injection. To comprehensively understand these changes, we present Pos(*G*) versus FWHM(*G*) data of 400 Raman spectra of GR before injection (black data points) and 346 Raman spectra after injection (blue data point)

© 2024 The Author(s). Advanced Healthcare Materials published by Wiley-VCH GmbH

21922659, 0, Downloaded from https://onlinelibrary.wiley.com/doi/10.1002/adhm.202401783 by Cnr Roma, Wiley Online Library on [04/02/2025]. See the Terms and Conditions (https://onlinelibrary.wiley.com/terms-and-conditions) on Wiley Online Library for rules of use; OA articles are governed by the applicable Creative Commons License

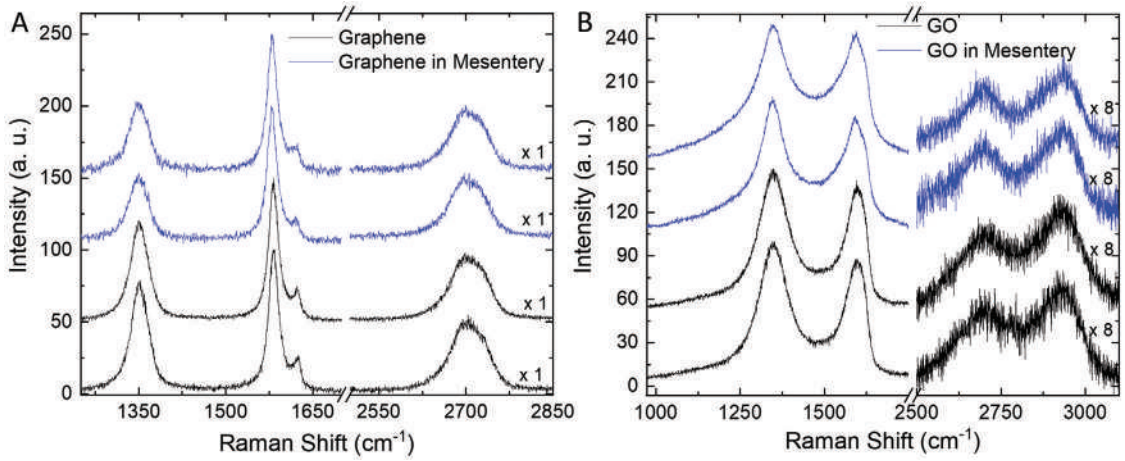

Figure 9. Representative Raman spectra from control graphene and GO before and after injection into the swine mesentery tissue. A) Representative Raman spectra of control graphene ink and graphene in the mesentery (Mes) tissue (Mes_Graphene – Mes) are shown in black and blue traces, respectively. B) Similarly, representative Raman spectra of control GO and GO in the mesentery (Mes) tissue (Mes_GO – Mes) are shown in black and blue traces, respectively.

into the mesentery tissue, in **Figure** 10A. The FWHM(*G*) versus *I(D)/I(G)* data of the same Raman spectra are presented in Figure 10B. The blue data points with error bars represent the mode of the statistical distributions of *I(D)/I(G)*, FWHM(*G*), and Pos(*D*), fitted using skew-normal distributions, before and after injection into the mesentery tissue. The error bars indicate the FWHM of the distributions. The Pos(*G*) of GR, before injection into mesentery tissue, is observed at ≈1582.92 cm^{-1}. After injection into mesentery, it decreases to ≈1581.06 cm^{-1}. This change (ΔPos(*G*) ≈−1.86 cm^{-1}) indicates average doping ≈2.33 × 10^{12} cm^{-269} in the graphene before injection, which is removed from the graphene after injection into the mesentery tissue. This doping may arise from FBS, the protein used to prepare the GR suspension. Strain can also lead to a negative ΔPos(*G*). However, in such cases, the ratio of change in the Raman shift of 2D peak (ΔPos(*2D*)) and ΔPos(*G*) is ≈2.2 cm^{-167}.[68] We observe ΔPos(*2D*)/ΔPos(*G*) ≤ 1, which rules out the possibility of strain being the primary contributor in the observed negative ΔPos(*G*) (Figure S15, Supporting Information). The removal of the doping would lead to a positive change (ΔFWHM(G)) in the FWHM(G) by ≈9.15 cm^{-1} in the graphene[69] in the mesentery tissue, compared to graphene suspension. However, we did not observe any change in the FWHM(G). This can only be possible if the expected positive change in the FWHM(G) is being compensated by the reduction in defect density[73] in graphene after injection into the tissues, possibly by breakages at the defect sites. Such reduction of defect is also evident in the observed reduction in I(D)/I(G) in the graphene in mesentery tissue. It is important to note that the D peak also appears from the graphene edges.[76,77] A reduction of I(D)/I(G) with unchanged FWHM(G) may also indicate the removal of smaller flakes from the tissue after injection. A quantitative analysis of

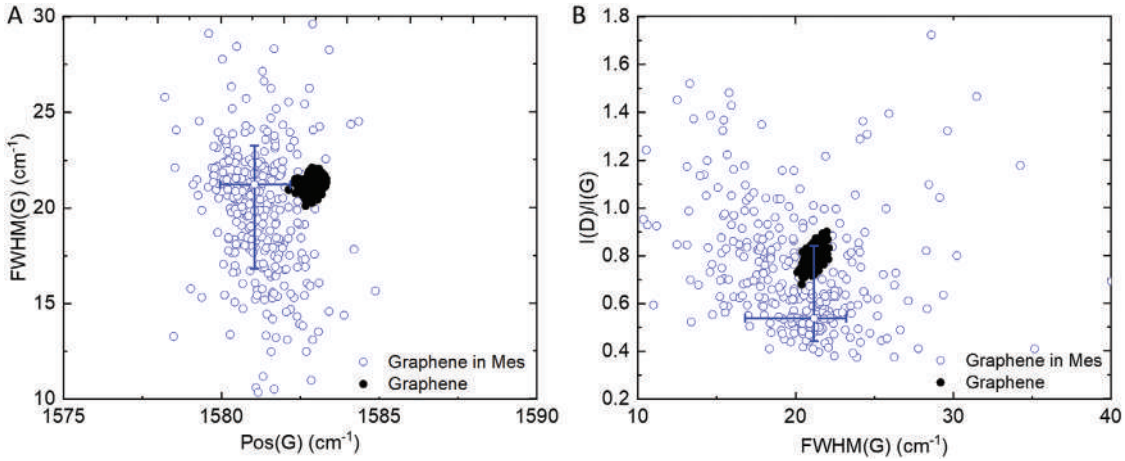

Figure 10. Statistical analysis of Raman signal of graphene before and after injection into mesentery tissue. A) Black (blue) and data points indicate FWHM(G) versus Pos(G) data of the Raman spectra of graphene before (after) injection into the mesentery tissue. The blue data point with the error bar indicates the value of the dataset's mode after injection. B) I(D)/I(G) versus FWHM(G) data of the Raman spectra of graphene before and after injection into the mesentery tissue is shown.

© 2024 The Author(s). Advanced Healthcare Materials published by Wiley-VCH GmbH

21922659, 0, Downloaded from https://onlinelibrary.wiley.com/doi/10.1002/adhm.202401783 by Cnr Roma, Wiley Online Library on [04/02/2025]. See the Terms and Conditions (https://onlinelibrary.wiley.com/terms-and-conditions) on Wiley Online Library for rules of use; OA articles are governed by the applicable Creative Commons License

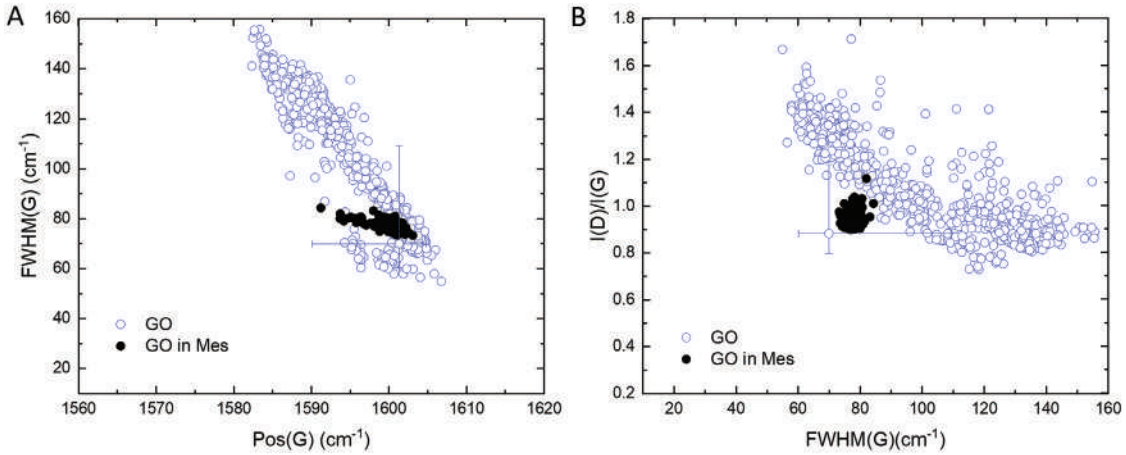

Figure 11. Statistical analysis of Raman signal of GO before and after injection into mesentery tissue. A) Black (blue) and data points indicate FWHM(G) versus Pos(G) data of the Raman spectra of GO before (after) injection into the mesentery tissue. The blue data point with the error bar indicates the value of the dataset's mode after injection. B) I(D)/I(G) versus FWHM(G) data of the Raman spectra of graphene before and after injection into the mesentery tissue is shown.

the reduction of defects and/or removal of the smaller flakes is difficult due to a complex interplay of defects and edges in the GR injected into the tissues. Moreover, the data points from graphene in mesentery appear to be more scattered compared to the control graphene suspension. This indicates an increased inhomogeneity in GR after injection into the mesentery.

The Raman spectra of GO (Figure 9B) are observed to be consisting of a broad *G* peak ≈1600 cm^{-1} and a *D* peak ≈1350 cm^{-1}. In microcrystalline graphene, $I(D)/I(G)$ increases with increasing defect concentration following Tuinstra and Koenig's relation,[78] which fails at a higher disorder concentration. In this regime, $I(D)/I(G)$ decreases with increasing disorder.[64,73] Observed $I(D)/I(G)$ ≈1 and large FWHM(*G*) observed from GO indicate extremely large defect density in our GO samples, which is quantitatively discussed later. At such a large defect density, the *G* and *D* peaks of GO are well fitted using BWF and Lorentzian functions, respectively.[64] Here, the peak position of the BWF function represents Pos(*G*). The Pos(*G*) versus FWHM(*G*) data of 400 Raman spectra of GO before injection (black data points) and 656 Raman spectra after injection (blue data point) into the mesentery tissue are presented in **Figure 11A**. The FWHM(*G*) versus $I(D)/I(G)$ data of the same Raman spectra are presented in Figure 11B. The blue data points with error bars indicate the mode values of these parameters after injection. The Pos(*G*), FWHM(*G*), and $I(D)/I(G)$ of the GO, before injection into mesentery tissue, are observed to be ≈1584 cm^{-1},≈77 cm^{-1}, and ≈1, respectively. Using FWHM(*G*) and $I(D)/I(G)$, the defect density in GO before injection can be estimated to be $0.5–1 \times 10^{12}$ cm^{-2}[73]. The Pos(*G*) versus FWHM(*G*) data after injection into mesentery can be best described as a dispersion around a line with a negative slope, where the Pos(*G*) decreases as FWHM(*G*) increases. This behavior arises due to the increase in bond disorder in the GO after injection.[64] As expected, FWHM(*G*) versus $I(D)/I(G)$ data after injection is also observed to be dispersed along a line with a negative slope. Interestingly, $I(D)/I(G)$ is observed to be increased (for the same value of FWHM (G)) after injection. This also indicates the disappearance of smaller nanocrystals after injection into the tissue. Additionally, we observed an increased inhomogeneity in GO inside mesentery, similar to GR.

Conventional histological evaluation was also performed. As displayed in Figure S10, Supporting Information, no polymorphonuclear cells, such as neutrophils, eosinophils, and basophils, around GBMs were identified in GR- and GO-exposed animals. Two distinct histopathological patterns were detected in the GO- and GR-exposed pigs. First, in the GO group, focal macrophage aggregates, representing the most prominent cell component, were found intermixed with a few lymphocytes. Moreover, chronic inflammation developed into another distinctive pattern known as granuloma around the GO aggregates (Figure S10, Supporting Information). In this case, activated macrophages evolved into multinucleate giant cells, forming well-defined nodules surrounded by an outer fibroblastic reactive wall (Figures S10 and S11, Supporting Information). Histologically, variable numbers of lymphocytes with few macrophages were instead observed around the GR aggregates, and no granulomas were detected. GO aggregates, regardless of their dimension, seemed completely incorporated by macrophages, whereas GR aggregates accumulated within the mesentery but were not included by inflammatory cells. As displayed in **Figure 12**, immunophenotyping confirmed the presence of CD163+ macrophages around GO aggregates and revealed that a few T cells (CD3+) were recruited in this group, whereas many T cells and a few macrophages were recruited around GR aggregates. Few B cells (CD79+) were detected around either GR or GO aggregates (Figure 12).

3. Discussion and Conclusions

3.1. Biocompatibility of Pristine Graphene and GO Using Swine as a Close-to-Human Animal Model

Considerable scientific and research activities have been devoted in recent years to the study of possible biomedical applications of GBMs due to their promising intrinsic properties. However, a critical step to ensure their safe exploitation in biomedicine

© 2024 The Author(s). Advanced Healthcare Materials published by Wiley-VCH GmbH

21922659, 0, Downloaded from https://onlinelibrary.wiley.com/doi/10.1002/adhm.202401783 by Cnr Roma, Wiley Online Library on [04/02/2025]. See the Terms and Conditions (https://onlinelibrary.wiley.com/terms-and-conditions) on Wiley Online Library for rules of use; OA articles are governed by the applicable Creative Commons License

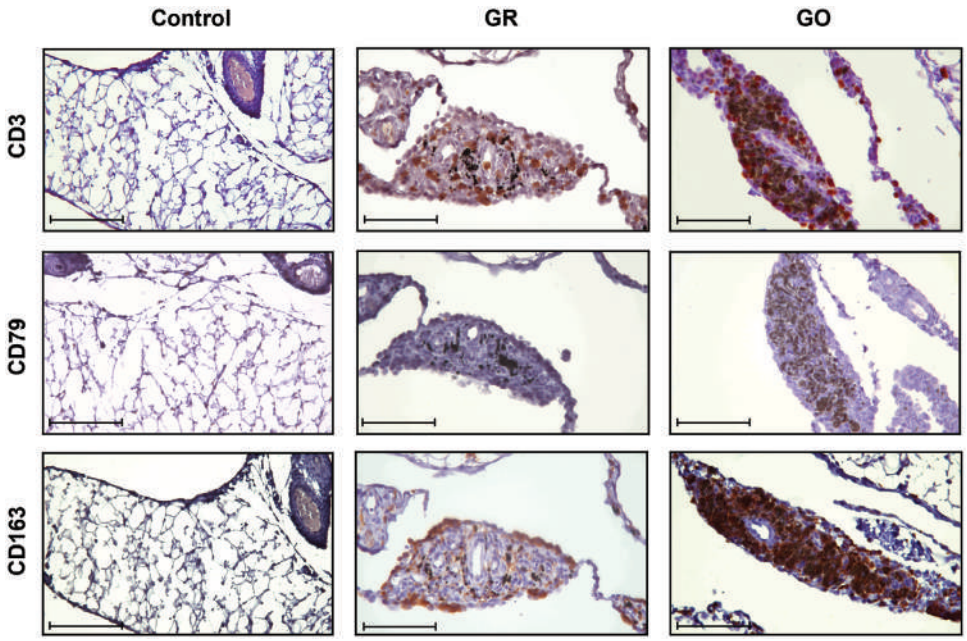

Figure 12. Immunohistochemistry of mesentery 21 days after injection. Inflammatory cell immunophenotyping was performed in paraffin-embedded sections of mesentery collected 21 days post-injection. CD163, CD3, and CD79 were used as markers for activated macrophages, and T and B lymphocytes, respectively. Immune reactions were visualized by 3,3′-diaminobenzidine chromogen, Mayer's hematoxylin counterstaining. Images of three representative pigs, one from each group (control, GR, GO), are displayed. Scale bar, 100 µm.

is to evaluate their biocompatibility. The biological interactions of GBMs are determined by material-intrinsic parameters, including the number of layers, lateral dimensions, and the C/O ratio.[5,79] The present study aimed at providing a comprehensive view of the in vivo biocompatibility of two GBMs using a large animal model. We compared the impact of pristine graphene prepared according to state-of-the-art techniques to graphene oxide, both sterile, endotoxin-free, and with similar lateral sizes (average lateral size of ≈0.6 µm). Ex vivo and in vivo analyses were performed using swine, which is one of the most important animal species used in translational research, due to the many anatomical and immunological analogies shared with humans.[28,29,80] Swine as a biomedical model presents numerous advantages, and it is valuable in bridging the gap between pre-clinical and clinical studies on GBMs. In addition, GBMs biocompatibility was evaluated through a wide variety of approaches and multiple advanced imaging techniques.

3.2. Ex Vivo Assays: Pristine Graphene and GO Lack Toxicity and Trigger the Release of Pro-Inflammatory Cytokines by Pig Immune Cells

In the initial part of the work, the interaction of GR and GO with ex vivo swine blood cells was assessed, and the impact of these materials on cellular and molecular parameters was evaluated. Hemolysis and platelet aggregations are undesirable effects mediated by GBMs at high concentrations,[15,16] thus, we first incubated high doses (50 µg mL^{-1}) of these materials with swine whole blood. Our results showed that neither GR nor GO altered any of the tested parameters (platelet numbers, red and white blood cells parameters), suggesting a lack of toxic effect on RBCs, platelets, or leukocytes. Hemolytic assay using swine RBCs was also applied to evaluate the biocompatibility of these compounds before in vivo administration. High doses of GO but not of GR induced a minor albeit statistically significant increase in the number of RBCs lysed after 24 h of incubation. Nevertheless, the induced hemolysis was modest, and statistical significance was detected only at high doses of GO (75 µg mL^{-1}). Thus, our results suggested a good biocompatibility of both GBMs tested.

Then, the interaction of GBMs with leukocytes was further investigated through ex vivo experiments on PBMCs, assessing their effect on cell viability and cytokine release. Both materials did not show cytotoxic effect on PBMCs, but they stimulated the release of pro-inflammatory cytokines. These results are in agreement with our previous studies in human PBMCs, where GO induced overexpression of pro-inflammatory factors in PBMCs.[9] Interaction of GR and GO with macrophages was also investigated, considering that they are the immune population involved in defense against foreign invaders.[56] We observed that both GBMs induce a small but statistically significant cytotoxic effect in these cells, and these findings are in agreement with our previous results: blood monocytes were the most affected lymphocyte population in terms of viability after exposure to carbon-based materials.[2,10] As expected, our data revealed that both GBMs triggered a sustained release of pro-inflammatory cytokines (IL-1β, IL-6, and IL-12) by swine macrophages. These findings suggested that GMBs polarized swine macrophages toward an M1 phenotype in agreement with previous results in human cells.[9]

© 2024 The Author(s). Advanced Healthcare Materials published by Wiley-VCH GmbH

21922659, 0, Downloaded from https://onlinelibrary.wiley.com/doi/10.1002/adhm.202401783 by Cnr Roma, Wiley Online Library on [04/02/2025]. See the Terms and Conditions (https://onlinelibrary.wiley.com/terms-and-conditions) on Wiley Online Library for rules of use; OA articles are governed by the applicable Creative Commons License

3.3. In Vivo Assays: Absence of Systemic Toxicity of Pristine Graphene and GO After i.p. Injection

Next, to obtain a better understanding of the toxicological and immunomodulatory properties of GBMs, GR and GO were administered to 12-week-old pigs using the i.p. route. As stated above, this route has been widely used for toxicity testing, thanks to the fast absorption of injected materials or drug delivery, especially in chemotherapy in patients with primary peritoneal surface malignancies.[40] Intraperitoneal chemotherapy can also be useful in patients with gynecological and gastrointestinal cancers.[81] Peritoneal spread of tumors is indeed one of the main problems in cancer management due to deterioration in patients' quality of life and shortened survival. Intraperitoneal chemotherapy can help maximize tumor penetration and reduce systemic toxic effects.[84] Nanomedicine can facilitate drug delivery in targeted tissues, and it was recently described that multi-drug loaded PEGylated nanodiamonds injected intraperitoneally in mice were able to inhibit pancreatic tumor growth and metastasis.[83] Recent work has shown that the i.p. route is more effective than the conventional i.v. route in terms of delivering miRNA/siRNA-loaded nanoparticles to retroperitoneal pancreatic tumor tissues of mice, with an almost 15-fold higher tumor accumulation i.p. compared to i.v. injected mice.[84] Consequently, this route was selected for our pilot study in order to evaluate the potential biomedical application of these GBMs.

First, biocompatibility and the impact of GR and GO on immune cells early post-administration (24 h, T_1) were investigated using PCR arrays. The expression of 84 immune-related genes in circulating PBMCs was assessed, including several pro-inflammatory and anti-inflammatory cytokines and members of the tumor necrosis factor family genes. Our results showed that very few genes were modulated in treated animals (IL1A and FASLG for GR; IL16, IL21, BMP2, AIMP2, LTB for GO).

Then, the toxicity of GR and GO was evaluated at different time points post-injection through complete blood count, chemical profile, and serum protein electrophoresis. Nanoparticles, in fact, might cause hemolysis, affecting the membrane integrity of RBCs by mechanical or reactive oxygen species damage or by platelet aggregation and activation.[16] In our study, all the hematological parameters evaluated indicated that neither GO nor GR caused systemic inflammatory, toxic, or pro-coagulant responses. Not only hemocompatibility but also GO and GR impact on the function of major organ systems were evaluated. GMBs might indeed affect liver or kidney functionality, with consequent changes in hepatic and renal injury markers,[17] and it was recently described that a PEGylated GO, administered i.v. at 4 mg mL^{-1}, led to acute anaphylactic reactions in non-human primates, characterized by increased circulating levels of both hepatic function indicators (AST, ALT) and cardiac indicators (CK) .[53] A complete analysis of GBMs biocompatibility and toxicity is a mandatory step for their exploitation in biomedicine, thus, in our study, multiple serum markers were monitored to evaluate both liver and renal functions.[60] We observed no differences in serum AST, GGT, bilirubin, triglycerides, and cholesterol parameters, indicating that both GR and GO do not cause liver damage or functional impairment. Absence of abnormalities in urea, creatinine, sodium, and potassium indicated that both GBMs did not impair renal filtration functions and their ability to maintain electrolyte balance. In addition, a lack of depression in total protein and albumin levels suggested that both the liver's synthetic capability and the kidney's filtration ability were not impaired. No differences between treated and control pigs were detected also in CPK levels throughout the study, indicating that both GBMs did not cause cardiac damage. Overall, both GR and GO appeared to be well-tolerated in pigs. Interestingly, an escalation trend for ALP values was indeed observed in the GO-group. Increases of ALP values are often correlated with systemic inflammation, and several GO agglomerates surrounded by inflammatory cells were observed in the mesentery of GO-treated pigs. In this pilot study a single dose of 0.5 mg Kg^{-1} (corresponding to 6.8 mg m^{-2}) GBMs was injected into pigs, thus in the future the impact of prolonged exposure and/or repeated administrations of GO should be evaluated to achieve a more complete assessment of its biocompatibility.

Immunomodulatory properties of GR or GO through the study were also evaluated, investigating circulating cytokine levels and expression of an early activation marker on PBMCs. Cytokines can be biomarkers of nanomaterial immunotoxicity, and pro-inflammatory cytokines might lead to inflammation-mediated toxicity.[6] In our study, no differences between groups in terms of pro-inflammatory (IL-1β, IL-2, IL-6, TNF-α), anti-inflammatory (IL-10) or other cytokine (IL-2, IL-12) levels were observed at any time post-injection (T_1-T_4). These data, alongside electrophoretic results, highlighted the absence of an inflammatory reaction. In addition, no differences between groups were observed in terms of expression of CD25 (early activation marker) on circulating PBMCs at several times post-inoculation.

These GBMs altered a few of the tested parameters, and overall, these data indicate the absence of systemic toxicity of these materials or a negative impact on the animal's immune system. It is important, however, to note that the present results, although they are encouraging, cannot automatically be extrapolated to all other types of GBMs. Indeed, we compared the behavior of one representative form of GO and one form of water-dispersed pristine graphene, which has been exfoliated in FBS. Previous work using a similar form of graphene has shown that such materials are enriched for certain serum proteins, including apolipoprotein A1,[85] while we have not addressed the potential role of surface-adsorbed proteins. Such proteins may play a role in terms of biological interactions with cells, including, in particular, cells of the immune system. In another study, BALB/c mice and *Macaca fascicularis* monkeys were i.v. injected with GO (25 mg Kg^{-1} in mice and 4 mg Kg^{-1} in monkeys), and the animals were monitored up to 28 and 90 days, respectively.[53] Although GO showed no acute or long-term adverse effects in most animals, the authors noted non-negligible anaphylactic reactions and even death in some cases. Seven out of 121 tested mice died ≈1–12 h post-exposure (mortality rate 5.8%), while for primates, one out of 5 monkeys died ≈1.5 h post-exposure (mortality rate 20%). The authors documented elevated levels of immunoglobulin E and severe lung injury in the dead animals, suggesting the GO-induced acute anaphylactic reactions.[53] Differences between the latter study and our study are not limited to the administration route (i.e., intravenous versus intraperitoneal) but may certainly also have to do with differences between the tested GBMs. Besides the lateral size of GO, which in the study of Lin et al. is in the range of 20–80 nm, the most striking difference

© 2024 The Author(s). Advanced Healthcare Materials published by Wiley-VCH GmbH

21922659, 0, Downloaded from https://onlinelibrary.wiley.com/doi/10.1002/adhm.202401783 by Cnr Roma, Wiley Online Library on [04/02/2025]. See the Terms and Conditions (https://onlinelibrary.wiley.com/terms-and-conditions) on Wiley Online Library for rules of use; OA articles are governed by the applicable Creative Commons License

is due to the chemical modification of their GO with a ramified polyethylene glycol. This polymer masks the surface of GO, affording a material that is not comparable to our unmodified GBMs, leading to clear differences in the biological responses.

3.4. Clusters of Pristine Graphene and GO Observed in the Mesentery but Not in Vital Organs

Biodistribution of the GBMs and their possible impact on vital organs were then assessed. Necroscopy was thus performed 21 days post-injection, and we observed numerous small aggregates of GBMs scattered in the peritoneum of the GO-treated pigs. These results are in agreement with previous studies in rats, where GO aggregates of diverse dimensions were described in the mesentery,[21,23,26] with the finest aggregates observed in liver and spleen serosa. GR aggregates were instead invisible to the naked eye and were revealed only by histological examination. Accumulation of these GBMs in the spleen or liver might have affected these organs, and overall accumulation of nanomaterials in the liver or spleen is indeed considered as one of the major barriers to translating nanomedicines, as these organs are responsible for clearance of exogenous compounds.[86]

Hematoxylin and eosin (H&E) staining was performed to determine histopathological changes in both liver and spleen, and no sign of necrosis, inflammation, hyperplasia, atrophy, hypertrophy, fibrosis, or hemorrhage of these organs was observed in either GO- or GR-exposed animals. In addition, no GR or GO accumulated in these organs, and histological results suggest that GBMs were not able to penetrate retroperitoneal organs through adventitia, as previously described.[21] Moreover, no signs of damage were observed in the kidneys of exposed pigs. To further investigate GBM distribution in tissues, TA imaging, and Raman mapping experiments were performed. TA can detect signals from GBMs within cells/tissues with very high specificity and in a short acquisition time (down to tens of microseconds per pixel), thus allowing the scanning of relatively large areas with high spatial resolution.[62] On the other hand, TA cannot precisely determine the chemical and physical properties of GBMs (e.g., doping and number of layers) that can be easily detected by spontaneous Raman, which in turn requires much longer acquisition time (down to fractions of a second per pixel) preventing high-resolution imaging of large tissue areas. Raman mapping was previously used to determine the presence of GR in various organs in mice.[87] Here, we have demonstrated that GR and GO are only present inside the treated mesentery tissues of swine and are absent in the spleen, kidney, and liver tissues of swine. The coupling of these two complementary approaches allowed us to confirm the presence or absence of GR and GO in relatively large tissue regions and, in parallel, to precisely characterize their features in the biological context. Both GO and GR clusters were surrounded by immune cells, suggesting that the host immune system played a role in restricting the progression of these foreign materials outside the mesentery, avoiding damage to vital organs. Similar results were observed in a previous study in mice. Hence, Sydlik and colleagues found that GO was moderately compatible in vivo following intraperitoneal administration, with an inflammatory reaction in response to implantation consistent with a typical foreign body reaction.[88] The authors noted that GO injection triggered the recruitment of monocytes, macrophages, and multinucleated giant cells in the mesentery, but no damage was observed to vital organs such as the liver or spleen.[88]

Previous studies in mice reported instead that GBMs were accumulated in cells of the RES in either liver or spleen,[19,25] with Kupffer cells being engulfed with GBMs.[17,25] In the liver, Kupffer cells are the main cell type involved in nanomaterial uptake, followed by hepatic B cells and liver sinusoidal endothelial cells.[70] We did not find any evidence of GBMs engulfed by macrophages or other cell types in either the spleen or liver, and differences might also be due to the different GBMs doses injected into animals: 6.8 mg m^{-2} in our study and 60, 90, or 150 mg m^{-2} in mice with GO accumulation in RES.[17,19,25] Future studies should investigate whether prolonged exposure and/or repeated administrations of GO or GR will overcome host defenses and lead to the accumulation of these GBMs in the liver or spleen.

In agreement with those studies, we observed that macrophages were the main cell type surrounding GO aggregates in the mesentery. As stated above, macrophages are phagocytic cells involved in foreign materials up-take,[56] and in fact, similar results were reported in rats intraperitoneally injected with GOs, where peritoneal macrophages efficiently internalized both large or small GO sheets.[26] GO clusters were surrounded by this cell type, and we observed that large GO agglomerates induced the formation of granulomas. These findings are in contrast with previous data,[26] where GOs of diverse dimensions were not able to induce a granulomatous response in the mesothelium and exacerbated inflammatory response in the peritoneum, with recruitment of monocytic cells, lymphocytes, neutrophils, and eosinophils. We observed only a modest recruitment of T cells and no neutrophils around GO clusters, nevertheless, cells involved in the granuloma formation and fibrotic capsule were detected. These differences might be linked to different properties of GOs used in our and in the aforementioned study, for example, the lateral dimension of the materials used. In fact, a more recent study described the presence of peri-bronchiolar granulomas in mice after intranasal administration of another GO, and these granulomas were localized in areas with significant agglomeration of GBMs.[89] The granulomatous response incited by GO is a consequence of the inability of macrophages to destroy GO-aggregates, and it is likely to have a protective function; it is an attempt of the host to segregate and destroy the foreign material.[90] Macrophage recruitment was observed in the present study for both GBMs. Nevertheless, T cells were the main cell types detected around GR aggregates. We observed that GO and GR triggered a distinct inflammatory response, as demonstrated by the different histopathological patterns observed. A recent study demonstrated that PEGylated GO stimulated a strong immunological response to macrophages due to the interaction between these materials and macrophage membrane.[91] On the contrary, our immunohistochemical analysis revealed that GR aggregates were not internalized by macrophages, and this might be correlated with the modest recruitment of phagocyte cells. One might speculate that certain GR properties might hinder uptake by the mononuclear phagocyte system, and this should be better investigated in further studies.

© 2024 The Author(s). Advanced Healthcare Materials published by Wiley-VCH GmbH

21922659, 0, Downloaded from https://onlinelibrary.wiley.com/doi/10.1002/adhm.202401783 by Cnr Roma, Wiley Online Library on [04/02/2025]. See the Terms and Conditions (https://onlinelibrary.wiley.com/terms-and-conditions) on Wiley Online Library for rules of use; OA articles are governed by the applicable Creative Commons License

Finally, we investigated whether the GBMs under study underwent biotransformation within the host tissues. Biotransformation is indeed a protective mechanism, an attempt by the host to transform foreign materials to less reactive ones. Previous studies in mice reported structural changes of GO within mice tissues.[26,89,92] Rodriguez and colleagues performed Raman mapping to analyze the progressive biotransformation of GO into less graphitic structures following intranasal administration.[89] Moreover, evidence for splenic capture and biotransformation of GO was obtained following i.v. administration to mice.[92] Evidence for biodegradation of GR in lung, liver, kidney, and spleen following i.v. administration was also provided, and spleen-bound GR showed an almost complete amorphization over a period of several months.[87] Similarly, in our study, Raman spectra revealed an increased inhomogeneity of both GR and GO upon injection into the mesentery tissues, suggesting that these GBMs were transformed in vivo.

3.5. Modest Local Tissue Reaction without Systemic Toxicity After i.p. Injection of Pristine Graphene and GO Set the Foundation for Their Biomedical Applications

Notwithstanding, our pilot study using a porcine model showed that intraperitoneally injected GR or GO formed aggregates in the peritoneum without harmful systemic effects or vital organ damage. Our results confirm their potential for applications in bioimaging, photothermal therapy, or photodynamic therapeutic agents. GO injection resulted in the formation of several granulomas scattered in the mesentery, whereas GR also induced a modest local reaction in the peritoneum. Thus, our preliminary data on GR are promising in regard to its potential use in biomedical applications. However, the abovementioned study in monkeys[53] cautions that the route of administration needs to be taken into careful consideration. Most importantly, although several previous studies reported that pristine graphene presented higher toxicity compared to functionalized graphene,[13,16,17] the present study using GR prepared in FBS with excellent aqueous dispersibility showed remarkable biocompatibility ex vivo as well as in vivo.

In conclusion, in this pilot study, the ex vivo and in vivo biocompatibility and potential immunological impact of water-dispersible pristine graphene and graphene oxide were investigated using a close-to-human animal model. Indeed, tolerance and potential immunomodulatory properties of both materials were assessed using swine as a model due to the strong anatomical, physiological, and immunological analogies between pigs and humans.[28,29,33,35] Through a compendium of results, our study revealed that GBMs triggered a modest local tissue reaction without systemic toxicity. This work in swine set the foundation for the future translation of these materials, including pristine graphene, in clinical settings.

4. Experimental Section

Preparation of Water-Dispersible Pristine Graphene: Graphite (Timrex KS25, Imerys) (200 mg) was suspended in fetal bovine serum (FBS) (1 mL) with no additives at an initial concentration of 200 g L^{-1}. The graphite suspension was then homogenized for 200 cycles at 2000 bar to ensure the exfoliation of graphite. After homogenization, the graphite was centrifuged for 1 h at 5000 rpm, resulting in a stable graphene suspension with a concentration of ≈10 g L^{-1}. The graphene was characterized using SEM, AFM, and Raman spectroscopy.

Preparation of Graphene Oxide: GO was synthesized following a modified Hummers' method[41] and obtained as a stable aqueous dispersion. Starting from the highly-oxidized GO with a lateral size higher than 10 µm, an aqueous dispersion of GO with a controlled size of ≈0.6 µm was obtained using the Mixa system (high speed after 5 cycles, 3 min of blender treatment per cycle) followed by HPH for one cycle. GO was extensively dialyzed against MilliQ water via a column system equipped with the endotoxin-free Polisseur Biopak, using Spectra/Por dialysis membrane (MWCO 12 000–14 000 Da) for more than 20 days to reach a pH of ≈4.5. The final concentration of GO is 3.85 mg mL^{-1}. GO was characterized by scanning electron microscopy (SEM), atomic force microscopy (AFM), X-ray photoelectron spectroscopy (XPS), and Raman spectroscopy.

Characterization: XPS analyses were performed on a Thermo Scientific K-Alpha X-ray photoelectron spectrometer with a basic chamber pressure of 10^{-8}–10^{-9} bar with an anode using Al Kα radiation (hn = 1486.6 eV). The C1s photoelectron binding energy was set at 284.5 ± 0.2 eV and used as a reference for calibrating the other peak positions. The samples were analyzed as powder. Spot size of 400 µm was used. The survey spectra are an average of 10 scans with a pass energy of 200.00 eV and a step size of 1 eV. The high-resolution spectra are an average of 10 scans with a pass energy of 50 eV and a step size of 0.1 eV. An ion gun was turned on during analysis. For each sample, the analysis was repeated three times. For the deconvolution, CasaXPS (Version 2.3.16 PR 1.6) program was used to interpret data based on the Gaussian e Lorentzian line shapes and the Shirley type background. SEM analyses were performed on a SEM SU9000 (Hitachi High Technologies Corporation, Tokyo, Japan). To prepare the SEM samples, a diluted dispersion of GO was dropped on SiO_2/Si substrate treated under ozone for a few minutes. AFM analyses were performed with SPM-9700HT (Shimadzu Scientific Instruments, Kyoto, Japan). The AFM samples were prepared by dropping a diluted GO and GR dispersion on a mica substrate.

Preparation of the Dispersions: In order to compare the toxicological and immunological impact, GR and GO were diluted in water with 10% FBS and glucose (5% w/v) at a final concentration of 1 mg mL^{-1}.

Sterility and Endotoxin Test: Sterility and endotoxin levels in GR and GO were estimated before injection. Sterility test was performed by plating GR and GO suspensions (100 µg mL^{-1}) on Luria Bertani (LB) agar plates and incubating them overnight at 37 °C. The formation of bacterial colonies was examined after 24 h incubation. The TNF-α expression test (TET)[42] was used to determine the endotoxin content of these GBMs. The cytotoxicity of these compounds on human monocyte-derived macrophages (HMDMs) was first evaluated. Specifically, PBMCs were isolated from buffy coats obtained from healthy human blood donors (Karolinska University Hospital, Stockholm) by density gradient centrifugation using Lymphoprep (STEMCELL Technologies). PBMCs were then positively selected for CD14 expression using CD14 MicroBeads (Miltenyi Biotec). To obtain HMDMs, CD14 monocytes were cultured in RPMI-1640 cell medium supplemented with 2 mM L-glutamine, 100 U mL^{-1} penicillin, 100 µg mL^{-1} streptomycin, and 10% heat-inactivated FBS, supplemented with 50 ng mL^{-1} recombinant M-CSF (PeproTech, UK) for 4 days. HMDMs were exposed to GR and GO at the concentrations of 5, 25, 50, and 75 µg mL^{-1} for 24 h, and cell viability was assessed by the lactate dehydrogenase (LDH) release assay. To determine the endotoxin content of the materials, HMDMs were incubated with GR and GO at the non-toxic dose of 25 µg mL^{-1} in the presence or absence of the specific LPS inhibitor, polymyxin B sulfate (10 µM) for 24 h. LPS (0.01 µg mL^{-1}) was used as a positive control. The TNF-α concentration in the cell culture supernatants was quantified by ELISA (Mabtech AB).

Swine PBMC Purification, Cryopreservation and Culture: Swine PBMCs were prepared by diluting 15 mL of EDTA blood in 15 mL of phosphate-buffered saline (PBS), layering it over 20 mL of Histopaque-1077 (Sigma), and centrifuging it at 600 g for 30 min at room temperature (RT), without braking, in a rotating bucket centrifuge. PBMCs were aspirated from the plasma-histopaque interface and washed three times in PBS by centrifuga-

© 2024 The Author(s). Advanced Healthcare Materials published by Wiley-VCH GmbH

21922659, 0, Downloaded from https://onlinelibrary.wiley.com/doi/10.1002/adhm.202401783 by Cnr Roma, Wiley Online Library on [04/02/2025]. See the Terms and Conditions (https://onlinelibrary.wiley.com/terms-and-conditions) on Wiley Online Library for rules of use; OA articles are governed by the applicable Creative Commons License

tion at 1000 g for 5 min at 4 °C.[43] For in vitro experiments, swine PBMCs were cultured in RPMI 1640 medium completed with 10% of inactivated fetal bovine serum and 100 U mL^{-1} penicillin and 100 µg mL^{-1} streptomycin (complete RPMI), using 12 well plates (2×10^6 $well^{-1}$). For in vivo experiments, swine PBMCs were stained immediately for flow cytometry analysis or re-suspended in QIAzol or cryopreserved for later analysis. PBMCs were adjusted to a density of $1 \times 10^{7,}$ and an aliquot (6×10^7) was re-suspended in cold (4 °C) 10% dimethyl sulfoxide (DMSO) in FBS and transferred to four pre-cooled (4 °C) cryotubes (1.5 mL $tube^{-1}$). Tubes were placed in a −80 °C freezer for 24 h and then transferred to a liquid nitrogen storage container.[43]

Animal Procedures and Sample Collection: Thirteen 12-week-old pigs (*Sus scrofa domesticus*), nine males and four females, were used for in vivo animal experiments. Pigs were an average size of 30 kg at the start of experiments. They were randomly divided into three groups, and then 2D materials were administered using an intraperitoneal route: five animals were injected with GR (0.5 mg Kg^{-1}), five with GO (0.5 mg Kg^{-1}), three with water 10% FBS (15 mL $animal^{-1}$, control group), all with 5% glucose w/v. Details on the group selection and gender are provided in Table S1, Supporting Information. Pigs were under anesthesia with Zoletil (tiletamine-zolazepam) during nanomaterial injection. Ultrasounds (Sonosite, Amsterdam, Netherlands) were used to monitor GR and GO administration into the peritoneal cavity. The portable multi-parameter veterinary monitor iPm12Vet (Mindray, Shenzhen, Hong Kong) was used to monitor vital parameters (electrocardiogram, body temperature, oxygen saturation, blood pressure, and respiratory rate) in anesthetized animals, starting 5 min before nanomaterial administration until animal awakening. After a single intraperitoneal injection of GR or GO suspensions in pigs, blood was collected over time during the animal experiment: T_0 (pre-injection), T_1 (24 h post-injection), T_2 (7 days post-injection), T_3 (14 days post-injection), T_4 (21 days post-injection, before euthanasia). At each time point, 18 mL of whole blood was collected (16 mL using EDTA as an anticoagulant) for toxicity investigation and to assess the impact of these materials on the immune system.

Serum was collected from 2 mL of whole blood without anticoagulant to monitor changes in chemical profile and globulin levels, as described in Section 2.9. EDTA blood was used to perform a complete blood count (CBC) (1 mL), as described in Section 2.8, and for PBMCs purification (15 mL), as described in Section 2.3. 3×10^6 PBMCs were stained immediately for flow cytometry analysis (as described in Section 2.10), 6×10^7 PBMCs were cryopreserved (as described in Section 2.3), and 4×10^7 PBMCs were re-suspended in QIAzol (Qiagen) (1×10^7 mL^{-1}). Samples in QIAzol were stored for 7 days at −20 °C and then at −80 °C until analyzed. Plasma was also collected and stored immediately at −80 °C until analysis of circulating cytokines levels. 21 days post-injection, the pigs were first anesthetized with intramuscular administration of Zoletil (tiletamine-zolazepam), then euthanized using Tanax (Intervet, Italy). Immediately after death, samples from the spleen, peritoneum, liver, and kidney were collected and fixed neutral buffered 4% (v/v) formalin and then embedded in paraffin blocks for histology and immunohistochemistry (see Section 2.12).

Hemocompatibility Assays: Hemolysis test was conducted following previously used protocols.[44] Red blood cells (RBCs) were purified from swine heparinized blood by centrifugation at 200×g for 5 min to remove serum. Resulting RBCs were then washed in sterile PBS 1× three times and diluted 10× with the same solution. The hemolytic activity of GR or GO was determined by incubation of these compounds with the RBC suspension (0.1 mL, ≈2×10^8 RBCs mL^{-1}) at different concentrations (5, 25, 50, and 75 µg mL^{-1}) in a final volume of 1 mL. 24 h later, intact RBCs were removed by centrifugation for 5 min at 500 g. The absorbance of hemoglobin released in the supernatant was read with an Epoch microplate reader (BioTek, Winooski, USA) at 570 nm with the absorbance at 620 nm as a reference.

Cell Viability Assay: Impact of GR and GO on swine PBMC viability ex vivo was evaluated using a non-radioactive cytotoxicity assay, as previously described.[45] Swine PBMCs were left untreated or cultured in the presence of GR or GO (both at 50 µg mL^{-1}). LDH levels in culture supernatants indicative of a loss of plasma membrane integrity were quantified using a Cytotox 96 Non-Radioactive Cytotoxicity Assay (Promega, Madison, WI, USA). A lysis solution provided by the manufacturer was used as the positive control, whereas untreated PBMCs were used as the negative control. Absorbance was read at 492 nm using an Epoch microplate reader (BioTek, Winooski, USA).

Cytokine Secretion Assay: PBMCs for ex vivo experiments were cultured in the presence or absence of 50 µg mL^{-1} of GR or GO for 24 h, and then culture supernatants were harvested and stored at −80 °C until cytokine/chemokine analysis. All experiments used LPS (2 µg mL^{-1}) as a positive control. Levels of IL-1β, IL-2, IL-4, IL-6, IL-10, IL-12, TNF-α were determined using Porcine Cytokine/Chemokine Magnetic Bead Panel Multiplex assay (Merck Millipore, Darmstadt, Germany) and a Bioplex MAGPIX Multiplex Reader (Bio-Rad, Hercules, CA, USA), according to the manufacturer's instructions, as previously described.[43,45] Plasma samples were collected over time during the in vivo animal experiment (pre-injection and 1, 7, 14, and 21 days post-injection) and were stored at −80 °C until cytokine detection assay; assays followed the same procedure described above.

Blood Count: CBC was performed on swine EDTA blood samples collected over time during the in vivo animal experiment (pre-injection and 1, 7, 14, and 21 days post-injection). The samples were analyzed within 3 h of sampling. CBC was also performed on ex vivo swine blood cells: EDTA blood was treated with 50 µg mL^{-1} of GR or GO or left untreated and incubated at 37 °C for 24 h. The main blood parameters were evaluated using an ADVIA 2120 analyzer (Siemens).[39] We reported the number of red cells (1×10^6 μL^{-1}), the number of platelets (1×10^3 μL^{-1}), and the number of total white blood cells (1×10^3 μL^{-1}), then divided into neutrophils, lymphocytes and monocytes. We analyzed the hematocrit (HCT), the volume percentage of red blood cells in the blood, and the amount of hemoglobin (HGB) expressed in g dL^{-1}. The mean corpuscular hemoglobin (MCH) and its concentration (MCHC) were evaluated. Last, we examined the red blood cell distribution width (RDW), which is the variation in the cellular volume of the red blood cell population, and the hemoglobin distribution width (HDW), which measures the heterogeneity of the red cell hemoglobin concentration. The list of parameters and their reference range are reported in Table S2, Supporting Information.

Biochemistry and Serum Protein Electrophoresis: Swine serum samples were collected over time during the in vivo animal experiment (pre-injection and 1, 7, 14, and 21 days post-injection). Whole blood without anticoagulant (2 mL) was centrifuged at 3000 g for 10 min, and serum was immediately analyzed to monitor changes in chemical profile and globulin levels.[39] An automated spectrophotometer (EXL 200, Siemens, Monaco, Germany) was used to quantify albumin, alkaline phosphatase (ALP), bilirubin, calcium, phosphorus, creatinine, total proteins, gamma-glutamyl transferase (GGT), aspartate transferase (AST), urea, cholesterol, creatine phosphokinase (CPK), and triglycerides in serum samples. SEBIA G26 (Interlab, Rome, Italy) was instead used to assess serum protein levels (g dL^{-1}) and percentages of albumin, α1-globulin, β-globulin, γ-globulin. The list of parameters and their reference range are reported in Table S2, Supporting Information.

PBMCs Gating Strategy and Activation Markers on Flow Cytometry: Swine PBMCs were collected over time during animal experiments, and 3×10^6 were stained immediately to monitor changes in the main lymphocyte population and activation marker expression. The cells were transferred into 5 mL round bottom tubes (Corning) (1×10^6 PBMCs $tube^{-1}$), stained with monoclonal antibodies specific for surface markers for 15 min at RT, and then washed with PBS containing 2% of FBS. The monocytes were differentiated using mouse anti-human CD14-PerCP-Cy5.5 (Tuk4; Miltenyi Biotec), whereas main lymphocyte populations were discriminated using the following monoclonal antibodies (moAb): mouse anti-bovine CD21-PE (CC51; Bio-rad), mouse anti-pig CD3-PerCP-Cy5.5 (BB23-8E6-8C8; BD Pharmigen), mouse anti-pig CD4-FITC (74-12-4; BD Pharmigen), mouse anti-pig CD8-PE (76-2-11; BD Pharmigen). Monoclonal antibodies anti-human CD14 (Tuk4) and anti-bovine CD21 (CC51) cross-react with pig.[46,47] The percentages of B cells ($CD21^+CD3^-$), T cells ($CD3^+CD21^-$), subsequently divided in cytotoxic ($CD3^+CD8^{high}CD4^-$), naïve T helper ($CD3^+CD8^-CD4^+$), memory T helper ($CD3^+CD8^{low}CD4^+$), NK cells ($CD3^-CD8^+CD4^-$) and monocytes ($CD14^+$) were monitored over

© 2024 The Author(s). Advanced Healthcare Materials published by Wiley-VCH GmbH

21922659, 0, Downloaded from https://onlinelibrary.wiley.com/doi/10.1002/adhm.202401783 by Cnr Roma, Wiley Online Library on [04/02/2025]. See the Terms and Conditions (https://onlinelibrary.wiley.com/terms-and-conditions) on Wiley Online Library for rules of use; OA articles are governed by the applicable Creative Commons License

time. The expression of CD25 (activation marker) was assessed using first mouse anti-pig CD25 (K231.3B2, Bio-rad) and subsequent staining with BV421 rat anti-mouse IgG1 (A85-1, BD Horizon). The percentage of CD25 surface activation marker expression on gated monocytes ($CD14^+$), B cells, T cells (subsequently divided in cytotoxic, naïve T helper, memory T helper), and NK cells was monitored pre-injection and 1, 7, 14, 21 days post-injection. Surface-stained cells were resuspended in PBS 0.1% formalin and then analyzed on BD FACS Celesta (BD Biosciences, Franklin Lakes, NJ, USA), and 100 000 live monocytes or lymphocytes were acquired. Analysis of data was performed using BD FACS Diva Software (BD Biosciences) by exclusion of doublets and then gating on viable monocytes or lymphocytes. Defined lymphocyte subpopulation and monocytes were then gated upon, and their expression of CD25 was assessed, as previously described.[43]

RNA Extraction and PCR Array Analysis: PCR arrays for 84 genes related to the immune response were measured on nine samples from T_0 and T_1 (24 h) time points: three pigs of the control group (#10, #11, #12), three GR treated (#01, #08, #09), three GO treated (#02, #04, #06) (see Table S1, Supporting Information). RNA was extracted from the PBMCs using the RNeasy Mini Kit (QIAGEN). The concentration and quality of RNA were determined by the NanoDrop spectrophotometer (Thermo Fisher). Pure RNA has a A260/A280 absorption ratio of ≈2.1, and A260/A230 is higher than 1.8. All RNA samples were found to be of high quality. Total RNA (500 ng) was used for cDNA synthesis using the RT2 First Strand Kit (QIAGEN). Real-time PCR was then conducted using the RT2 Profiler PCR Array for immune-related genes (QIAGEN, Cat. No. 330 231 PASS-021ZA). The data analysis was performed using the GeneGlobe Data Analysis Center available at QIAGEN (https://geneglobe.qiagen.com/us/analyze). The list of genes is shown in Table S3, Supporting Information (according to information provided by the manufacturer). The relative gene expression levels were calculated using the classical and widely adopted $2^{-\Delta\Delta CT}$ method.[48] Student's t-test was used to evaluate the statistical differences, and a statistically significant difference was set as $p < 0.05$. The log transformation was performed on fold change and p values. Significantly up- and down-regulated genes were marked in red and blue, respectively. Thresholds of twofold change are indicated in the shaded area. The plots were generated in GraphPad Prism (v. 8.2.0). Non-supervised hierarchical clustering was performed to indicate the co-regulated genes across the individual samples and groups.[49] The magnitude of gene expression was determined by calculating the $2^{-\Delta CT}$ for each gene and normalizing to the average $2^{-\Delta CT}$ of all genes across the samples. The distance metric was employed to convert data points into clusters, and the linkage method was used to join the clusters to form a tree.

Histopathology and Immunohistochemistry: Paraffin-embedded tissue blocks were cut into 5 µm thick sections and stained with hematoxylin and eosin (H&E) (Bio-optica, Milan, Italy) to determine tissue histopathological changes. Sections were examined under a light microscope (Leica, Wetzlar, Germany) coupled with a digital camera. The identification of macrophages ($CD163^+$), T lymphocytes ($CD3^+$), and B lymphocytes ($CD79^+$) in situ was performed using immunohistochemistry, as previously described.[39] Briefly, 5–7 µm thick sections were deparaffinized and rehydrated in ethanol before staining. For CD163 antigen retrieval, sections were immersed in a solution of 0.01 M citric acid (pH 6.1) and treated in a pressure cooker (Biocare, Milan, Italy) (110 °C × 15 min). For CD3 and CD79 antigen retrieval, sections were immersed in pH 9 Tris Buffer EDTA solution and then treated in a pressure cooker (110 °C × 15 min). Sections were incubated overnight at 4 °C using the following primary antibodies: anti-porcine monoclonal antibody (mAb) CD163 (EDHu-1, Bio-rad), anti-human CD79αcy mAb (HM57, Dako Agilent, Santa Clara, CA, USA) and a rabbit polyclonal anti-human CD3 (Dako Agilent). Immune reactions were then visualized by 3,3′-diaminobenzidine chromogen solution (Dako Agilent).

Transient Absorption and Raman Mapping: Both transient absorption (TA) imaging and Raman mapping experiments were performed on samples collected 21 days post-injection from six tested subjects: two pigs of the control group (#10, #12), two GR-treated (#01, #09), two GO-treated (#04, #06). Paraffin-embedded tissue blocks were cut into 10-µm thick sections and deparaffinized, modifying a previously optimized protocol.[50] Briefly, tissue slices, mounted onto 0.17 mm thick glass coverslips, were dewaxed by two baths of hexane 95% (Merck KGaA), two baths of ethanol absolute (Merck KGaA), and a final bath of ethanol 95%, followed by air drying for 2 h.

TA imaging experiments were performed using a two-color TA configuration coupled to a point-scanning microscope.[51] A train of pump pulses at 1040 nm with »200-fs duration and 80 MHz repetition rate is synchronized and collinearly combined with a train of probe pulses at 780 nm with »100 fs duration. Pump and probe pulses are focused on the tissue slide by a 1.25 numerical aperture (NA) microscope objective (CFI Plan Apo IR 60XC WI, Nikon). At the sample plane, the pump and the probe beams are confined to a diameter of » 1 µm. The transmitted probe is collected with a second objective (CFI Apo Lambda S 60X Oil, NA = 1.4, Nikon), spectrally selected by a short-pass filter, and measured with a photodiode. An acousto-optic modulator modulates the pump beam at 1.6 MHz, and the pump-induced differential transmission (DT/T) of the probe is synchronously detected by a lock-in amplifier. The pixel dwell time used for TA imaging experiments was 1.2 ms, with the typical field of view of 300 × 300 µm. We also performed confocal micro Raman spectroscopy, using a HORIBA LabRAM Evolution Raman spectrometer, on the same samples, that is, GR- and GO-treated tissues, control tissues (without GR and GO treatment), and control GR and GO samples, which were used to treat the tissues. Four different kinds of tissues, that is, mesentery (mes), spleen, liver, and kidney, were investigated using confocal Raman spectroscopy using 514.5 nm laser wavelength, with a laser spot size ≈0.5 µm. 100× objective with 0.9 numerical aperture and 1800 mm^{-1} grating were used. We performed Raman mapping in a 20 µm × 20 µm area of the control tissues. Raman spectra of GR and GO before and after injection into the tissues were compared to understand the evolution of the physical parameters like strain, doping, and defects.

Statistical Analysis: Ex vivo experiments were performed in triplicate and repeated at least three times using different blood donor pigs. In vivo experiments were instead performed using 13 pigs, randomly divided into three groups: three animals in the control group (Group 1), five pigs exposed to GR (Group 2), and five animals exposed to GO (Group 3). The sample size for in vivo population was calculated following Viechtbauer and collaborators (2015),[52] assuming the baseline probability of observing a difference between groups is 0.05% (95% IC = 0.01–0.08). The completeness and consistency of the collected data, stored in an ad hoc database, were evaluated. The same statistical approach and methodology were applied to ex vivo and in vivo datasets. Shapiro-Wilk test was used to test the normal distribution of each independent variable. After assessing the baseline distribution of the whole blood parameter, biochemical profile, serum protein, and cytokines, quantitative variables were summarized as mean values, standard deviations (SD), median, and interquartile range, depending on the best representative measure. Differences between variables were evaluated by applying the T-Student or Kruskal-Wallis nonparametric tests. Repeated-measures mixed model has been applied using five time points (T_0 = pre-injection; T_1 = 1, T_2 = 7, T_3 = 14, T_4 = 21 days post-injection, respectively) the variable on which the data are repeated to test the hypothesis of equality of variances within-subjects and between-groups. Any possible interaction factor between parameters, time, and subject has been tested in the model. In addition to the estimates of the fixed effects (each parameter and time points), we get random effects. These are the variance of the intercepts and the residual variance, which correspond to the between-subject and within-subject variances. The level of $p < 0.05$ was considered significant for all the analyses, except for multiple comparisons, for which the Bonferroni correction was used (p-value/n° of contrast in the five groups: P<0.01). The software used to conduct the analysis was STATA/SE for Window, version 15 (StataCorp, College Station, TX, USA). For details on the analysis of the gene expression data, refer to Section 2.11.

Ethical Statement: For ex vivo experiments, whole blood was obtained from three human informed donors (25–50 years old) and three healthy swine (*Sus scrofa domesticus*) (6–24 months old). The in vivo experiment was performed instead using 13 healthy 12-week-old swine. Pigs were housed at the Experimental Station of Istituto Zooprofilattico della Sardegna (IZS della Sardegna, Sassari, Italy) and were allowed to

© 2024 The Author(s). Advanced Healthcare Materials published by Wiley-VCH GmbH

21922659, 0, Downloaded from https://onlinelibrary.wiley.com/doi/10.1002/adhm.202401783 by Cnr Roma, Wiley Online Library on [04/02/2025]. See the Terms and Conditions (https://onlinelibrary.wiley.com/terms-and-conditions) on Wiley Online Library for rules of use; OA articles are governed by the applicable Creative Commons License

acclimatize for 2 weeks before any experiments. The IZS della Sardegna Ethics Committee reviewed and approved all the protocols performed for swine experiments. The in vivo experiment was further authorized by the Italian Ministry of Health (Ministero della Salute) in accordance with the Italian D.Igs 26/2014 (protocol n.779/2019-PR). Human blood was collected from healthy adult donors at the Karolinska University Hospital, Stockholm, Sweden. The donors were approved and covered by insurance according to the regulations at the Karolinska University Hospital, and their identity was unknown to scientists performing experiments. These buffy coats containing white blood cells are considered a waste product after the red blood cells have been utilized for blood transfusions thus, the Ethical Committee for Human Studies in Stockholm previously notified that no specific ethical permit is required for in vitro (cell culture) studies of nanomaterials on cells derived from human buffy coats, such as the studies reported herein, since data cannot be traced back to individual blood donors (2006/900-31/3; decision 2006/3:8).

Supporting Information

Supporting Information is available from the Wiley Online Library or from the author.

Acknowledgements

Supported by the European Commission through the Graphene Flagship (grant agreement no. 785219), FLAG-ERA JTC Graphene 2015 (G-IMMUNOMICS project), STARS@UNIPD 2021 (DETECTION project), and the Italian Ministry of Health (IZS of Sardinia, project funded by national health funds). The authors would like to acknowledge Elisa Auneddu (University of Sassari, Sassari, Italy), Susanna Zinellu, and the Animal Services Unit (IZS della Sardegna, Sassari, Italy) for technical assistance during the study. The authors gratefully acknowledge the Centre National de la Recherche Scientifique (CNRS) through the International Research Project MULTIDIM between I2CT Unit and Okayama University, the International Center for Frontier Research in Chemistry (icFRC), and financial support from the Interdisciplinary Thematic Institute SysChem via the IdEx Unistra (ANR-10-IDEX-0002) within the program "Investissement d'Avenir." The authors also thank Lucas Jacquemin for his precious help on XPS analyses.

Open access publishing facilitated by Universita degli Studi di Padova, as part of the Wiley - CRUI-CARE agreement.

Conflict of Interest

The authors declare no conflict of interest.

Author Contributions

P.N., G.F., and L.G.D conceived and coordinated the study. A.B., B.F., G.F., and L.G.D wrote the paper with contributions from all authors. J.M. and Y.A.S. exfoliated and prepared the pristine graphene suspension under the supervision of A.F., N.Q.C., A.B., and Y.N. prepared GO. J.M. did the SEM study on the graphene ink. T.A. and A.F. performed the confocal Raman spectroscopy on the control and GO and graphene treated tissue samples. T.A. performed the Raman analysis. G.F. processed the samples during animal experiments, carried out ex vivo workflow cytometry analyses, and analyzed both the in vivo and the ex vivo data with the help of S.D.G, G.T., L.G., A.Y., G.C., L.S., and G.P. carried on the in vivo animal experiments, whereas M.G.C., G.T. performed necroscopy. M.G.C, S.M., and C.L. carried on H&E and immunohistochemistry analyses. G.P. and B.F. performed PCR arrays. A.D.P.G., R.V., D.P., and G.C. performed transmission electron microscopy. F.L. performed statistical analyses.

Data Availability Statement

The data that support the findings of this study are available from the corresponding author upon reasonable request.

Keywords

2D materials, biocompatibility, immune system, porcine model, toxicity

Received: May 14, 2024
Revised: August 30, 2024
Published online:

[1] A. Gazzi, L. Fusco, M. Orecchioni, S. Ferrari, G. Franzoni, J. S. Yan, M. Rieckher, G. Peng, M. A. Lucherelli, I. A. Vacchi, N. D. Q. Chau, A. Criado, A. Istif, D. Mancino, A. Dominguez, H. Eckert, E. Vázquez, T. D. Ros, P. Nicolussi, V. Palermo, B. Schumacher, G. Cuniberti, Y. Mai, C. Clementi, M. Pasquali, X. Feng, K. Kostarelos, A. Yilmazer, D. Bedognetti, B. Fadeel, et al., *J. Phys. Mater.* **2020**, *3*, 034009.
[2] L. Fusco, A. Gazzi, G. Peng, Y. Shin, S. Vranic, D. Bedognetti, F. Vitale, A. Yilmazer, X. Feng, B. Fadeel, C. Casiraghi, L. G. Delogu, *Theranostics* **2020**, *10*, 5435.
[3] G. Reina, J. M. González-Domínguez, A. Criado, E. Vázquez, A. Bianco, M. Prato, *Chem. Soc. Rev.* **2017**, *46*, 4400.
[4] J. Liu, L. Cui, D. Losic, *Acta Biomater.* **2013**, *9*, 9243.
[5] B. Fadeel, C. Bussy, S. Merino, E. Vázquez, E. Flahaut, F. Mouchet, L. Evariste, L. Gauthier, A. J. Koivisto, U. Vogel, C. Martín, L. G. Delogu, T. Buerki-Thurnherr, P. Wick, D. Beloin-Saint-Pierre, R. Hischier, M. Pelin, F. Candotto Carniel, M. Tretiach, F. Cesca, F. Benfenati, D. Scaini, L. Ballerini, K. Kostarelos, M. Prato, A. Bianco, *ACS Nano* **2018**, *12*, 10582.
[6] M. Elsabahy, K. L. Wooley, *Chem. Soc. Rev.* **2013**, *42*, 5552.
[7] M. Orecchioni, D. A. Jasim, M. Pescatori, R. Manetti, C. Fozza, F. Sgarrella, D. Bedognetti, A. Bianco, K. Kostarelos, L. G. Delogu, *Adv. Healthcare Mater.* **2016**, *5*, 276.
[8] S. P. Mukherjee, M. Bottini, B. Fadeel, *Front. Immunol.* **2017**, *8*, 00673.
[9] M. Orecchioni, D. Bedognetti, L. Newman, C. Fuoco, F. Spada, W. Hendrickx, F. M. Marincola, F. Sgarrella, A. F. Rodrigues, C. Ménard-Moyon, G. Cesareni, K. Kostarelos, A. Bianco, L. G. Delogu, *Nat. Commun.* **2017**, *8*, 1109.
[10] M. Orecchioni, V. Bordoni, C. Fuoco, G. Reina, H. Lin, M. Zoccheddu, A. Yilmazer, B. Zavan, G. Cesareni, D. Bedognetti, A. Bianco, L. G. Delogu, *Small Weinh. Bergstr. Ger.* **2020**, *16*, e2000123.
[11] T. Devasena, A. P. Francis, S. Ramaprabhu, in *Reviews of Environmental Contamination and Toxicology Volume*, *259*, (Ed. P. de Voogt), Springer International Publishing, Cham **2021**.
[12] C. Bussy, D. Jasim, N. Lozano, D. Terry, K. Kostarelos, *Nanoscale* **2015**, *7*, 6432.
[13] A. Sasidharan, L. S. Panchakarla, P. Chandran, D. Menon, S. Nair, C. N. R. Rao, M. Koyakutty, *Nanoscale* **2011**, *3*, 2461.
[14] Y. Zhang, S. F. Ali, E. Dervishi, Y. Xu, Z. Li, D. Casciano, A. S. Biris, *ACS Nano* **2010**, *4*, 3181.
[15] K.-H. Liao, Y.-S. Lin, C. W. Macosko, C. L. Haynes, *ACS Appl. Mater. Interfaces* **2011**, *3*, 2607.
[16] A. Sasidharan, L. S. Panchakarla, A. R. Sadanandan, A. Ashokan, P. Chandran, C. M. Girish, D. Menon, S. V. Nair, C. N. R. Rao, M. Koyakutty, *Small* **2012**, *8*, 1251.
[17] A. Sasidharan, S. Swaroop, C. K. Koduri, C. M. Girish, P. Chandran, L. S. Panchakarla, V. H. Somasundaram, G. S. Gowd, S. Nair, M. Koyakutty, *Carbon* **2015**, *95*, 511.
[18] Y. Li, Y. Liu, Y. Fu, T. Wei, L. Le Guyader, G. Gao, R.-S. Liu, Y.-Z. Chang, C. Chen, *Biomaterials* **2012**, *33*, 402.

© 2024 The Author(s). Advanced Healthcare Materials published by Wiley-VCH GmbH

21922659, 0, Downloaded from https://onlinelibrary.wiley.com/doi/10.1002/adhm.202401783 by Cnr Roma, Wiley Online Library on [04/02/2025]. See the Terms and Conditions (https://onlinelibrary.wiley.com/terms-and-conditions) on Wiley Online Library for rules of use; OA articles are governed by the applicable Creative Commons License

[19] K. Yang, L. Feng, X. Shi, Z. Liu, *Chem. Soc. Rev.* **2013**, *42*, 530.
[20] M. Orecchioni, R. Cabizza, A. Bianco, L. G. Delogu, *Theranostics* **2015**, *5*, 710.
[21] N. Kurantowicz, B. Strojny, E. Sawosz, S. Jaworski, M. Kutwin, M. Grodzik, M. Wierzbicki, L. Lipinska, K. Mitura, A. Chwalibog, *Nanoscale Res. Lett.* **2015**, *10*, 398.
[22] D. A. Jasim, S. Murphy, L. Newman, A. Mironov, E. Prestat, J. McCaffrey, C. Ménard-Moyon, A. F. Rodrigues, A. Bianco, S. Haigh, R. Lennon, K. Kostarelos, *ACS Nano* **2016**, *10*, 10753.
[23] B. Strojny, N. Kurantowicz, E. Sawosz, M. Grodzik, S. Jaworski, M. Kutwin, M. Wierzbicki, A. Hotowy, L. Lipinska, A. Chwalibog, *PLoS One* **2015**, *10*, e0144821.
[24] M. Ema, M. Gamo, K. Honda, *Regul. Toxicol. Pharm.* **2017**, *85*, 7.
[25] A. Ruiz, M. A. Lucherelli, D. Murera, D. Lamon, C. Ménard-Moyon, A. Bianco, *Carbon* **2020**, *170*, 347.
[26] A. F. Rodrigues, L. Newman, D. A. Jasim, I. A. Vacchi, C. Ménard-Moyon, L. E. Crica, A. Bianco, K. Kostarelos, C. Bussy, *Arch. Toxicol.* **2018**, *92*, 3359.
[27] G. A. Van Norman, *JACC BASIC Transl. Sci.* **2019**, *4*, 845.
[28] M. M. Swindle, A. Makin, A. J. Herron, F. J. Clubb, K. S. Frazier, *Vet. Pathol.* **2012**, *49*, 344.
[29] R. Pabst, *Cell Tissue Res.* **2020**, *380*, 287.
[30] S. P. Graham, R. K. McLean, A. J. Spencer, S. Belij-Rammerstorfer, D. Wright, M. Ulaszewska, J. C. Edwards, J. W. P. Hayes, V. Martini, N. Thakur, C. Conceicao, I. Dietrich, H. Shelton, R. Waters, A. Ludi, G. Wilsden, C. Browning, D. Bialy, S. Bhat, P. Stevenson-Leggett, P. Hollinghurst, C. Gilbride, D. Pulido, K. Moffat, H. Sharpe, E. Allen, V. Mioulet, C. Chiu, J. Newman, A. S. Afor, *Npj Vaccines* **2020**, *5*, 69.
[31] A. McNee, T. R. F. Smith, B. Holzer, B. Clark, E. Bessell, G. Guibinga, H. Brown, K. Schultheis, P. Fisher, S. Ramos, A. Nunez, M. Bernard, S. Graham, V. Martini, T. Chrun, Y. Xiao, J. C. Kash, J. K. Taubenberger, S. Elliott, A. Patel, P. Beverley, P. Rijal, D. B. Weiner, A. Townsend, K. E. Broderick, E. Tchilian, *J. Immunol.* **2020**, *205*, 648.
[32] P. P. Wibroe, A. C. Anselmo, P. H. Nilsson, A. Sarode, V. Gupta, R. Urbanics, J. Szebeni, A. C. Hunter, S. Mitragotri, T. E. Mollnes, S. M. Moghimi, *Nat. Nanotechnol.* **2017**, *12*, 589.
[33] G. T. Kozma, T. Mészáros, I. Vashegyi, T. Fülöp, E. Örfi, L. Dézsi, L. Rosivall, Y. Bavli, R. Urbanics, T. E. Mollnes, Y. Barenholz, J. Szebeni, *ACS Nano* **2019**, *13*, 9315.
[34] J. Szebeni, P. Bedocs, D. Csukás, L. Rosivall, R. Bünger, R. Urbanics, *Adv. Drug Delivery Rev.* **2012**, *64*, 1706.
[35] J. Szebeni, R. Bawa, *Biomedicines* **2020**, *8*, 82.
[36] P. Bedőcs, J. Szebeni, *Front. Immunol.* **2020**, *11*, 584966.
[37] J. Szebeni, *Drug Discov. Today* **2018**, *23*, 487.
[38] W. C. Zamboni, J. Szebeni, S. V. Kozlov, A. T. Lucas, J. A. Piscitelli, M. A. Dobrovolskaia, *Adv. Drug Delivery Rev.* **2018**, *136*, 82.
[39] L. G. Delogu, G. Vidili, E. Venturelli, C. Ménard-Moyon, M. A. Zoroddu, G. Pilo, P. Nicolussi, C. Ligios, D. Bedognetti, F. Sgarrella, R. Manetti, A. Bianco, *Proc. Natl. Acad. Sci.* **2012**, *109*, 16612.
[40] K. Chaudhary, S. Haddadin, R. Nistala, C. Papageorgio, *Curr. Clin. Pharmacol.* **2010**, *5*, 82.
[41] N. Morimoto, T. Kubo, Y. Nishina, *Sci. Rep.* **2016**, *6*, 21715.
[42] S. P. Mukherjee, N. Lozano, M. Kucki, A. E. Del Rio-Castillo, L. Newman, E. Vázquez, K. Kostarelos, P. Wick, B. Fadeel, *PLoS One* **2016**, *11*, e0166816.
[43] G. Franzoni, J. C. Edwards, N. V. Kurkure, D. S. Edgar, P. J. Sanchez-Cordon, F. J. Haines, F. J. Salguero, H. E. Everett, K. B. Bodman-Smith, H. R. Crooke, S. P. Graham, *Clin. Vaccine Immunol.* **2014**, *21*, 1410.
[44] C. Farace, P. Sánchez-Moreno, M. Orecchioni, R. Manetti, F. Sgarrella, Y. Asara, J. M. Peula-García, J. A. Marchal, R. Madeddu, L. G. Delogu, *Sci. Rep.* **2016**, *6*, 18423.
[45] G. Franzoni, S. Mecocci, C. G. De Ciucis, L. Mura, F. Dell'Anno, S. Zinellu, F. Fruscione, L. De Paolis, T. Carta, A. G. Anfossi, S. D. Guidici, E. Chiaradia, L. Pascucci, A. Oggiano, K. Cappelli, E. Razzuoli, *Front. Immunol.* **2023**, *14*, 1209898.
[46] C. N. Jacobsen, B. Aasted, M. K. Broe, J. L. Petersen, *Vet. Immunol. Immunopathol.* **1993**, *39*, 461.
[47] M. Sinkora, K. Stepanova, J. Sinkorova, *Dev. Comp. Immunol.* **2013**, *39*, 409.
[48] K. J. Livak, T. D. Schmittgen, *Methods* **2001**, *25*, 402.
[49] M. B. Eisen, P. T. Spellman, P. O. Brown, D. Botstein, *Proc. Natl. Acad. Sci. USA* **1998**, *95*, 14863.
[50] R. Vanna, C. Morasso, B. Marcinnò, F. Piccotti, E. Torti, D. Altamura, S. Albasini, M. Agozzino, L. Villani, L. Sorrentino, O. Bunk, F. Leporati, C. Giannini, F. Corsi, *Cancer Res.* **2020**, *80*, 1762.
[51] A. De la Cadena, F. Vernuccio, A. Ragni, G. Sciortino, R. Vanna, C. Ferrante, N. Pediconi, C. Valensise, L. Genchi, S. P. Laptenok, A. Doni, M. Erreni, T. Scopigno, C. Liberale, G. Ferrari, M. Sampietro, G. Cerullo, D. Polli, *APL Photonics* **2022**, *7*, 076104.
[52] W. Viechtbauer, L. Smits, D. Kotz, L. Budé, M. Spigt, J. Serroyen, R. Crutzen, *J. Clin. Epidemiol.* **2015**, *68*, 1375.
[53] Y. Lin, Y. Zhang, J. Li, H. Kong, Q. Yan, J. Zhang, W. Li, N. Ren, Y. Cui, T. Zhang, X. Cai, Q. Li, A. Li, J. Shi, L. Wang, Y. Zhu, C. Fan, *Nano Today* **2020**, *35*, 100922.
[54] J. Russier, E. Treossi, A. Scarsi, F. Perrozzi, H. Dumortier, L. Ottaviano, M. Meneghetti, V. Palermo, A. Bianco, *Nanoscale* **2013**, *5*, 11234.
[55] M. Orecchioni, C. Ménard-Moyon, L. G. Delogu, A. Bianco, *Adv. Drug Delivery Rev.* **2016**, *105*, 163.
[56] D. A. Hume, *Front. Immunol.* **2015**, *6*, 370.
[57] J.-H. Liu, S.-T. Yang, H. Wang, Y. Chang, A. Cao, Y. Liu, *Nanomedicine* **2012**, *7*, 1801.
[58] S. Zhang, K. Yang, L. Feng, Z. Liu, *Carbon* **2011**, *49*, 4040.
[59] M. Hadjidemetriou, S. McAdam, G. Garner, C. Thackeray, D. Knight, D. Smith, Z. Al-Ahmady, M. Mazza, J. Rogan, A. Clamp, K. Kostarelos, *Adv. Mater.* **2019**, *31*, 1803335.
[60] L. Moore, J. Yang, T. T. H. Lan, E. Osawa, D.-K. Lee, W. D. Johnson, J. Xi, E. K.-H. Chow, D. Ho, *ACS Nano* **2016**, *10*, 7385.
[61] D. Davydova, A. de la Cadena, D. Akimov, B. Dietzek, *Laser Photonics Rev.* **2016**, *10*, 62.
[62] J. Li, W. Zhang, T.-F. Chung, M. N. Slipchenko, Y. P. Chen, J.-X. Cheng, C. Yang, *Sci. Rep.* **2015**, *5*, 12394.
[63] D. Brida, A. Tomadin, C. Manzoni, Y. J. Kim, A. Lombardo, S. Milana, R. R. Nair, K. S. Novoselov, A. C. Ferrari, G. Cerullo, M. Polini, *Nat. Commun.* **2013**, *4*, 1987.
[64] A. C. Ferrari, J. Robertson, *Phys. Rev. B* **2000**, *61*, 14095.
[65] A. C. Ferrari, *Solid State Commun.* **2007**, *143*, 47.
[66] A. C. Ferrari, J. C. Meyer, V. Scardaci, C. Casiraghi, M. Lazzeri, F. Mauri, S. Piscanec, D. Jiang, K. S. Novoselov, S. Roth, A. K. Geim, *Phys. Rev. Lett.* **2006**, *97*, 187401.
[67] T. M. G. Mohiuddin, A. Lombardo, R. R. Nair, A. Bonetti, G. Savini, R. Jalil, N. Bonini, D. M. Basko, C. Galiotis, N. Marzari, K. S. Novoselov, A. K. Geim, A. C. Ferrari, *Phys. Rev. B* **2009**, *79*, 205433.
[68] J. Zabel, R. R. Nair, A. Ott, T. Georgiou, A. K. Geim, K. S. Novoselov, C. Casiraghi, *Nano Lett.* **2012**, *12*, 617.
[69] M. Lazzeri, F. Mauri, *Phys. Rev. Lett.* **2006**, *97*, 266407.
[70] S. Pisana, M. Lazzeri, C. Casiraghi, K. S. Novoselov, A. K. Geim, A. C. Ferrari, F. Mauri, *Nat. Mater.* **2007**, *6*, 198.
[71] A. Das, S. Pisana, B. Chakraborty, S. Piscanec, S. K. Saha, U. V. Waghmare, K. S. Novoselov, H. R. Krishnamurthy, A. K. Geim, A. C. Ferrari, A. K. Sood, *Nat. Nanotechnol.* **2008**, *3*, 210.
[72] D. M. Basko, S. Piscanec, A. C. Ferrari, *Phys. Rev. B* **2009**, *80*, 165413.
[73] L. G. Cançado, A. Jorio, E. H. M. Ferreira, F. Stavale, C. A. Achete, R. B. Capaz, M. V. O. Moutinho, A. Lombardo, T. S. Kulmala, A. C. Ferrari, *Nano Lett.* **2011**, *11*, 3190.

© 2024 The Author(s). Advanced Healthcare Materials published by Wiley-VCH GmbH

21922659, 0, Downloaded from https://onlinelibrary.wiley.com/doi/10.1002/adhm.202401783 by Cnr Roma, Wiley Online Library on [04/02/2025]. See the Terms and Conditions (https://onlinelibrary.wiley.com/terms-and-conditions) on Wiley Online Library for rules of use; OA articles are governed by the applicable Creative Commons License

[74] M. Bruna, A. K. Ott, M. Ijäs, D. Yoon, U. Sassi, A. C. Ferrari, *ACS Nano* **2014**, *8*, 7432.
[75] S. Tfaili, C. Gobinet, G. Josse, J.-F. Angiboust, M. Manfait, O. Piot, *Analyst* **2012**, *137*, 3673.
[76] C. Casiraghi, A. Hartschuh, H. Qian, S. Piscanec, C. Georgi, A. Fasoli, K. S. Novoselov, D. M. Basko, A. C. Ferrari, *Nano Lett.* **2009**, *9*, 1433.
[77] P. G. Karagiannidis, S. A. Hodge, L. Lombardi, F. Tomarchio, N. Decorde, S. Milana, I. Goykhman, Y. Su, S. V. Mesite, D. N. Johnstone, R. K. Leary, P. A. Midgley, N. M. Pugno, F. Torrisi, A. C. Ferrari, *ACS Nano* **2017**, *11*, 2742.
[78] F. Tuinstra, J. L. Koenig, *J. Chem. Phys.* **2003**, *53*, 1126.
[79] P. Wick, A. E. Louw-Gaume, M. Kucki, H. F. Krug, K. Kostarelos, B. Fadeel, K. A. Dawson, A. Salvati, E. Vázquez, L. Ballerini, M. Tretiach, F. Benfenati, E. Flahaut, L. Gauthier, M. Prato, A. Bianco, *Angew. Chem., Int. Ed. Engl.* **2014**, *53*, 7714.
[80] A. Summerfield, F. Meurens, M. E. Ricklin, *Mol. Immunol.* **2015**, *66*, 14.
[81] K. Jaaback, N. Johnson, T. A. Lawrie, *Cochrane Database Syst. Rev.* **2016**, *2016*, CD005340.
[82] M. D. Goodman, S. McPartland, D. Detelich, M. W. Saif, *J. Gastrointest. Oncol.* **2016**, *7*, 45.
[83] V. S. Madamsetty, K. Pal, S. Keshavan, T. R. Caulfield, S. K. Dutta, E. Wang, B. Fadeel, D. Mukhopadhyay, *Nanoscale* **2019**, *11*, 22006.
[84] Y. Xie, Y. Hang, Y. Wang, R. Sleightholm, D. R. Prajapati, J. Bader, A. Yu, W. Tang, L. Jaramillo, J. Li, R. K. Singh, D. Oupický, *ACS Nano* **2020**, *14*, 255.
[85] V. Castagnola, W. Zhao, L. Boselli, M. C. L. Guidice, F. Meder, E. Polo, K. R. Paton, C. Backes, J. N. Coleman, K. A. Dawson, *Nat. Commun.* **2018**, *9*, 1577.
[86] K. M. Tsoi, S. A. MacParland, X.-Z. Ma, V. N. Spetzler, J. Echeverri, B. Ouyang, S. M. Fadel, E. A. Sykes, N. Goldaracena, J. M. Kaths, J. B. Conneely, B. A. Alman, M. Selzner, M. A. Otrowski, O. A. Adeyi, A. Zilman, I. D. McGilvray, W. C. W. Chan, *Nat. Mater.* **2016**, *15*, 1212.
[87] C. M. Girish, A. Sasidharan, G. S. Gowd, S. Nair, M. Koyakutty, *Adv. Healthcare Mater.* **2013**, *2*, 1489.
[88] S. A. Sydlik, S. Jhunjhunwala, M. J. Webber, D. G. Anderson, R. Langer, *ACS Nano* **2015**, *9*, 3866.
[89] A. F. Rodrigues, L. Newman, D. Jasim, S. P. Mukherjee, J. Wang, I. A. Vacchi, C. Menard-Moyon, A. Bianco, B. Fadeel, K. Kostarelos, C. Bussy, *Adv. Sci. (Weinh)* **2020**, *7*, 1903200.
[90] A. J. Pagán, L. Ramakrishnan, *Annu. Rev. Immunol.* **2018**, *36*, 639.
[91] Z. Ding, N. Luo, H. Yue, Y. Gao, G. Ma, W. Wei, *J. Mater. Chem. B* **2020**, *8*, 6845.
[92] L. Newman, D. A. Jasim, E. Prestat, N. Lozano, I. de Lazaro, Y. Nam, B. M. Assas, J. Pennock, S. J. Haigh, C. Bussy, K. Kostarelos, *ACS Nano* **2020**, *14*, 10168.

© 2024 The Author(s). Advanced Healthcare Materials published by Wiley-VCH GmbH

21922659, 0, Downloaded from https://onlinelibrary.wiley.com/doi/10.1002/adhm.202401783 by Cnr Roma, Wiley Online Library on [04/02/2025]. See the Terms and Conditions (https://onlinelibrary.wiley.com/terms-and-conditions) on Wiley Online Library for rules of use; OA articles are governed by the applicable Creative Commons License